Ambiguity in the causes for decadal trends in atmospheric methane and hydroxyl

Alexander J. Turner[a,1], Christian Frankenberg[b,c,1], Paul O. Wennberg[b], and Daniel J. Jacob[a]

[a]School of Engineering and Applied Sciences, Harvard University, Cambridge, MA 02138; [b]Division of Geological and Planetary Sciences, California Institute of Technology, Pasadena, CA 91125; and [c]Jet Propulsion Laboratory, California Institute of Technology, Pasadena, CA 21109

Edited by Mark H. Thiemens, University of California, San Diego, La Jolla, CA, and approved December 28, 2016 (received for review September 26, 2016)

Methane is the second strongest anthropogenic greenhouse gas and its atmospheric burden has more than doubled since 1850. Methane concentrations stabilized in the early 2000s and began increasing again in 2007. Neither the stabilization nor the recent growth are well understood, as evidenced by multiple competing hypotheses in recent literature. Here we use a multispecies two-box model inversion to jointly constrain 36 y of methane sources and sinks, using ground-based measurements of methane, methyl chloroform, and the C^{13}/C^{12} ratio in atmospheric methane ($\delta^{13}CH_4$) from 1983 through 2015. We find that the problem, as currently formulated, is underdetermined and solutions obtained in previous work are strongly dependent on prior assumptions. Based on our analysis, the mathematically most likely explanation for the renewed growth in atmospheric methane, counterintuitively, involves a 25-Tg/y decrease in methane emissions from 2003 to 2016 that is offset by a 7% decrease in global mean hydroxyl (OH) concentrations, the primary sink for atmospheric methane, over the same period. However, we are still able to fit the observations if we assume that OH concentrations are time invariant (as much of the previous work has assumed) and we then find solutions that are largely consistent with other proposed hypotheses for the renewed growth of atmospheric methane since 2007. We conclude that the current surface observing system does not allow unambiguous attribution of the decadal trends in methane without robust constraints on OH variability, which currently rely purely on methyl chloroform data and its uncertain emissions estimates.

methane | renewed growth | hydroxyl | oxidative capacity | troposphere

Atmospheric methane (CH_4) is the second strongest anthropogenic greenhouse gas (1) and concentrations have been increasing for much of the past century (2) due, primarily, to increasing anthropogenic emissions. Atmospheric concentrations stabilized in the early 2000s (3) (hereafter referred to as the "methane stabilization") and began increasing again in 2007 (4, 5) (hereafter referred to as the "renewed growth"). There has been much speculation about the cause of these trends (3–24). Attribution has proved to be a difficult task in part because this period of renewed growth is characterized by a methane growth rate of ∼6 ppb/y, which represents a source–sink imbalance of only 3% [or an increase of 20 Tg/y compared with an estimated annual source of 550 Tg/y (13)].

Previous work investigating the trends in atmospheric methane has generally used observations of either atmospheric ethane or bulk carbon isotope ratios in atmospheric methane ($\delta^{13}CH_4$), in conjunction with methane observations, to provide additional constraints on the sources of methane. This is because ethane is coemitted with methane from fossil-fuel sources, which represent ∼62% of the ethane budget (25), and has been used to infer changes in methane emissions from fossil-fuel sources. Similarly, $\delta^{13}CH_4$ has been used to determine the sources governing atmospheric methane concentrations because different methane sources and sinks have distinct isotopic signatures.

However, previous works using ethane and $\delta^{13}CH_4$ have come to differing conclusions about the causes of the stabilization in the early 2000s and the renewed growth since 2007. For example, Kai et al. (9) used isotope measurements and attributed the methane stabilization to a reduction in microbial sources whereas Aydin et al. (8) and Simpson et al. (12) used ethane observations and attributed it to a reduction in fossil-fuel sources. Levin et al. (11) found isotope measurements to be inconclusive. Similarly, Hausmann et al. (17), Franco et al. (18), and Helmig et al. (19) used ethane observations and attributed part of the renewed growth to fossil-fuel sources whereas Schaefer et al. (16), Rice et al. (22), Nisbet et al. (23), and Schwietzke et al. (24) reached differing conclusions using isotope measurements. Schaefer et al. (16) concluded that fossil fuels did not contribute to the renewed growth, Nisbet et al. (23) concluded that fossil fuels were not a dominant factor, Rice et al. (22) concluded that fugitive fossil-fuel sources have increased since 2000, and Schwietzke et al. (24) concluded that fossil-fuel sources have not increased. This prompts the question: Why do many, apparently, plausible explanations disagree with each other?

Quantitative attribution of methane emissions to fossil-fuel sources at global scales using ethane is hampered by the large variability in methane-to-ethane emission ratios and recent increases in ethane sources that emit little methane (26, 27). Similarly, there is a large overlap in the signatures from fossil-fuel and nonfossil methane sources. Part of this overlap is because fossil-fuel sources are not strictly thermogenic in origin with more than 20% of the world's natural gas reserves coming from microbial activity (28–30). This overlap makes it difficult to draw quantitative conclusions about the methane sources, using

Significance

Recent trends in atmospheric methane are not well understood as evidenced by multiple hypotheses proposed to explain the stabilization of methane concentrations in the early 2000s and the renewed growth since 2007. Here we use a multispecies inversion to determine the cause of these decadal trends. The most likely explanation for the renewed growth in atmospheric methane involves a decrease in hydroxyl (OH), the main sink for atmospheric methane, that is partially offset by a decrease in methane emissions. However, we also demonstrate that the problem of attributing methane trends from the current surface observation network, including isotopes, is underdetermined and does not allow unambiguous attribution of decadal trends.

Author contributions: A.J.T. and C.F. designed research; A.J.T. and C.F. performed research; A.J.T. contributed new reagents/analytic tools; A.J.T., C.F., P.O.W., and D.J.J. analyzed data; and A.J.T., C.F., P.O.W., and D.J.J. wrote the paper.

The authors declare no conflict of interest.

This article is a PNAS Direct Submission.

Freely available online through the PNAS open access option.

Data deposition: The model and data reported in this paper have been deposited in GitHub, https://github.com/alexjturner/BoxModel_PNAS_20161223.

See Commentary on page 5324.

[1]To whom correspondence may be addressed. Email: aturner@fas.harvard.edu or cfranken@caltech.edu.

This article contains supporting information online at www.pnas.org/lookup/suppl/doi:10.1073/pnas.1616020114/-/DCSupplemental.

atmospheric measurements of $\delta^{13}CH_4$ on global scales (*SI Appendix*, section 1).

In addition, changes in the hydroxyl radical (OH), the main sink for atmospheric methane, complicate the issue. Previous work has used observations of methyl chloroform (CH_3CCl_3; abbreviated as "MCF") to provide constraints on global-to-hemispheric OH concentrations because the loss of methyl chloroform is controlled by OH (31–34). Recent work has shown how small increases in the OH sink can explain most of the methane stabilization (21).

Here we present a simple two-box (Northern and Southern Hemisphere) model to investigate the cause of the methane stabilization and renewed growth. Fig. 1 shows a schematic of the two-box model. The model simulates annual hemispheric concentrations of $^{12}CH_4$, $^{13}CH_4$, methyl chloroform, and OH. We use atmospheric observations of methane, $\delta^{13}CH_4$, and methyl chloroform to constrain annual hemispheric emissions of methane, the isotopic composition of the emissions, methyl chloroform emissions, and the OH abundance in a nonlinear, stochastic, Bayesian inversion.

Results

Most Likely Solution. The most likely solution, defined as the largest posterior probability sampled, found here is that the renewed growth is due to a decline in the OH sink, partially offset by a decrease in methane emissions. Similarly, the stabilization is explained by an increase in the OH sink offsetting an increase in methane emissions. Fig. 2 shows the most likely solution from our nonlinear inversion for the drivers of decadal trends in atmospheric methane and OH as well as the modeled methane, $\delta^{13}CH_4$, and methyl chloroform concentrations. The posterior model accurately represents the observed concentrations of all three species. This shows how changes of a few percent in the methane sources and sinks can explain all of the observed hemispheric-scale variability in methane and methyl chloroform. The large uncertainty in isotopic signatures (*SI Appendix*, section 1) makes it difficult to draw quantitative conclusions from the isotopic composition of Northern and Southern Hemispheric methane sources.

In the most likely solution the renewed growth in methane is, counterintuitively, explained by a reduction in methane emissions. We find an ∼25-Tg/y decrease in global methane emissions from 2003 to 2016, during the period of renewed growth that started in 2007. This decrease in methane emissions is offset by an ∼7% decrease in global mean OH over the same period, which is constrained by methyl chloroform observations. The combination of this decrease in methane emissions and OH results in an increase in atmospheric methane concentrations, observed in both hemispheres.

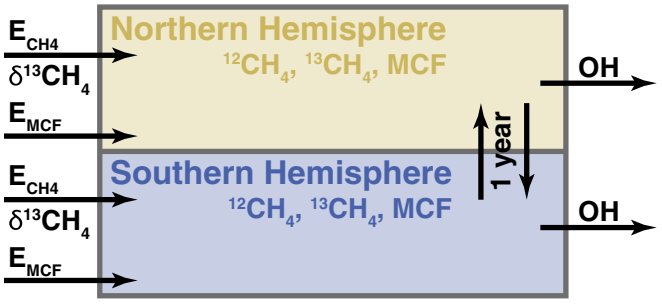

Fig. 1. Schematic of the two-box model. Inputs are annual hemispheric OH anomalies, methyl chloroform emissions, methane emissions, and $\delta^{13}CH_4$ for the methane emissions. Outputs are annual hemispheric concentrations of methyl chloroform, methane, and the $\delta^{13}CH_4$ of atmospheric methane. Interhemispheric exchange time is 1 y.

In this solution, we find an ∼35-Tg/y increase in methane emissions from 1993 to 2003 and an ∼7% increase in global mean OH from 1991 to 2000, with the bulk of the methane emission increase occurring in the Northern Hemisphere. The rate of increase in the methane emissions slows after about 1998, resulting in relatively stable atmospheric methane concentrations. Northern Hemispheric isotope concentrations do not exhibit any systematic changes during this period.

The isotopic compositions of the Northern and Southern Hemispheric methane sources (Fig. 2, *Middle Right*) are, largely, decoupled from the changes seen in the methane emissions and OH. The Northern Hemispheric methane emissions undergo modest changes whereas the isotopic composition of those emissions fluctuate about −52.5‰. Conversely, the Southern Hemispheric methane emissions remain largely unchanged from 1980 to 2016 whereas the isotopic composition decreases by about 2‰ from 1990 (when publicly available isotope measurements began) to 2015.

The OH anomalies derived here are consistent with previous work examining global mean OH (21, 31–34). In particular, Montzka et al. (31), Rigby et al. (33), and McNorton et al. (21) used methyl chloroform observations to derive anomalies in global mean OH. Fig. 3, *Top* shows that their OH anomalies exhibit a similarity to the OH anomalies found here. Patra et al. (34) found that the interhemispheric ratio of OH has been roughly constant from 2004 to 2011 (0.97 ± 0.12). Prather et al. (32) used observations of methyl chloroform to derive a methane lifetime of 9.1 ± 0.9 y whereas our global mean methane lifetime from 1980 to 2016 is 9.2 ± 0.2 y. The consistency between the results presented here and past findings is not particularly surprising because our work uses many of the same methyl chloroform datasets and prior emissions estimates as previous work.

This most likely solution is found to be robust to small perturbations in the prior error variance parameters for methane emissions and OH anomalies (*SI Appendix*, section 4.1), interhemispheric exchange times (*SI Appendix*, section 4.4), and alternate observation operators (*SI Appendix*, section 4.2). However, we find the amplitude of the changes in methane emissions and OH anomalies is strongly sensitive to the methyl chloroform reaction constant with OH (*SI Appendix*, section 4.5). Whereas the exact magnitude of our most likely solution changes in the different sensitivity tests, the general spatiotemporal pattern of increasing methane emissions and OH anomalies in the mid-1990s and decreasing methane emissions and OH anomalies from 2000 to present is robust to small perturbations but not large perturbations (as we present in the following sections).

Assuming Fixed OH Concentrations. We performed a sensitivity test (Fig. 4) where the inversion assumed time-invariant OH concentrations (global mean OH concentration of 1×10^6 molec/cm^3), thus linearizing the problem. The agreement with the observations is largely unchanged whereas methane emissions exhibit a fundamentally different temporal pattern. Here, we find that the renewed growth since 2007 is due to an ∼20-Tg/y increase in global methane emissions with each hemisphere contributing ∼10 Tg/y. The isotopic composition of the methane emissions is almost unchanged from the full nonlinear inversion, even though the methane emissions are radically different. MCF observations are reconciled through changes to the uncertain MCF emissions.

The only discernible difference between the simulated concentrations in the full nonlinear case and this sensitivity test with fixed OH concentrations is in the first 5 y of the $\delta^{13}CH_4$ concentrations when there are no observations (Fig. 4, *Left*). The consistency of the isotopic compositions indicates that simulating the $\delta^{13}CH_4$ observations is largely unaffected by changes in the methane emissions or OH concentrations and that the $\delta^{13}CH_4$ observations are providing constraints only on the isotopic compositions of the sources; it does not indicate that this

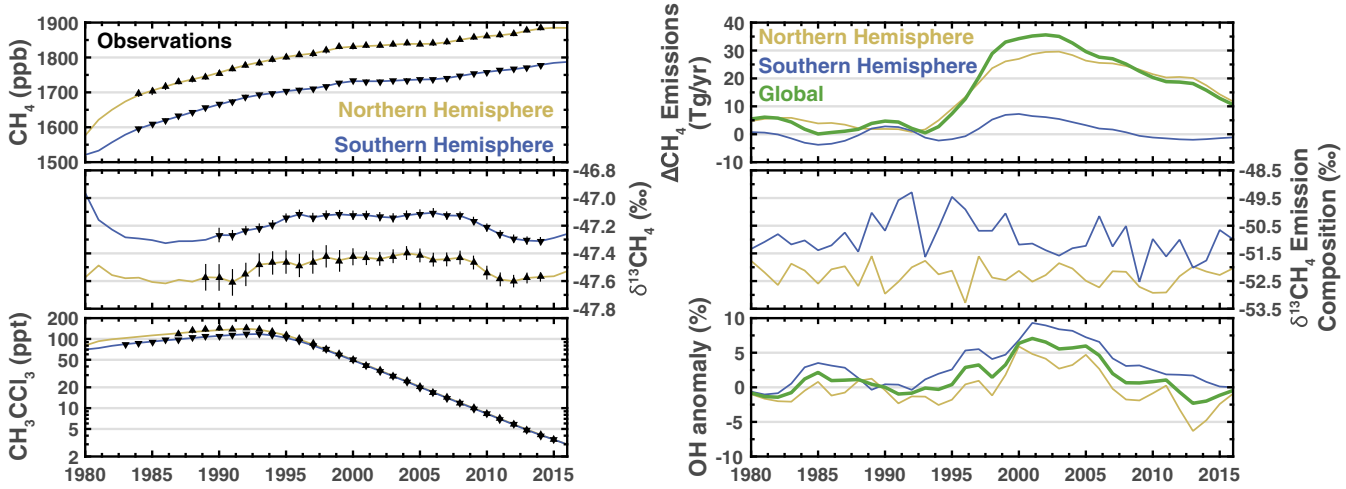

Fig. 2. Most likely solution. *Left* column shows observed (black triangles) and modeled (solid lines) concentrations of atmospheric CH_4 (*Top*), $\delta^{13}CH_4$ (*Middle*), and methyl chloroform (*Bottom*). The Northern Hemisphere is yellow and the Southern Hemisphere is blue. *Right* column shows the methane emissions (plotted as a deviation from the constant prior emissions; *Top*), the isotopic composition of the methane emissions (*Middle*), and the OH anomaly relative to a global mean concentration of 1×10^6 molecules (molec)/cm^3 (*Bottom*).

spatiotemporal pattern in the isotopic compositions is a robust feature. This difference in the first 5 y of $\delta^{13}CH_4$ concentrations is due to a slightly different treatment of the prior distribution for the initial conditions (*Materials and Methods*).

Assuming Fixed Methane Emissions. As an extreme test, we performed an additional sensitivity study (Fig. 5) where the inversion assumed that methane emissions were time invariant (global methane emissions of 550 Tg/y), also linearizing the problem. Only modest changes to the OH concentrations are needed to explain the observed methane concentrations with fixed methane emissions and a small divergence in Northern and Southern Hemispheric OH can explain changes in the interhemispheric methane difference. The renewed growth is explained by an ∼3–5% decrease in global mean OH from 2005 to 2016. However, this sensitivity test does require larger changes to the methyl chloroform emissions (*SI Appendix*, Fig. S4), relative to the full nonlinear inversion. Again, the isotopic composition of the methane emissions is almost unchanged from the full nonlinear inversion and is identical to the isotopic composition of the methane emissions from the sensitivity test with fixed OH concentrations.

Assuming the methane emissions are fixed implicitly places a constraint on the magnitude of the interannual variability of the global mean OH concentration. This is because an increase (decrease) in the OH anomaly could be offset by an increase (decrease) in the methane emissions to satisfy the observational record. As such, assuming the methane emissions are a fixed parameter (as opposed to a parameter to be estimated) in an inversion solving for global mean OH limits the potential interannual variability of global mean OH.

There are no discernible differences between the simulated concentrations in the two sensitivity tests and, as with the fixed OH sensitivity test, the only difference between the simulated concentrations in the full nonlinear case and this sensitivity test is in the first 5 y of the $\delta^{13}CH_4$ concentrations (Figs. 4, *Left* and 5, *Left*).

Discussion and Conclusions

We performed a nonlinear Bayesian inversion to infer the most likely set of drivers of decadal trends in atmospheric methane and OH. Based on our assumptions (Table 1), we find that decreasing OH concentrations is the most likely explanation for the renewed growth since 2007, with methane emissions actually decreasing during that period. This result is robust to small perturbations in our prior assumptions but not to large perturbations. The isotopic composition of the Southern Hemispheric methane sources in our most likely solution decreased by ∼1‰ during this period whereas the emissions decreased by ∼10 Tg/y. This would indicate that the isotopically heavy sources in the Southern Hemisphere (such as biomass burning) may have decreased whereas the isotopically light sources remained constant. There is evidence from the satellite record of CO pointing to a decrease in Southern Hemispheric biomass burning since 2001 (35) but some of the decrease in CO could be due to anthropogenic sources (36). The isotopic composition of the Northern

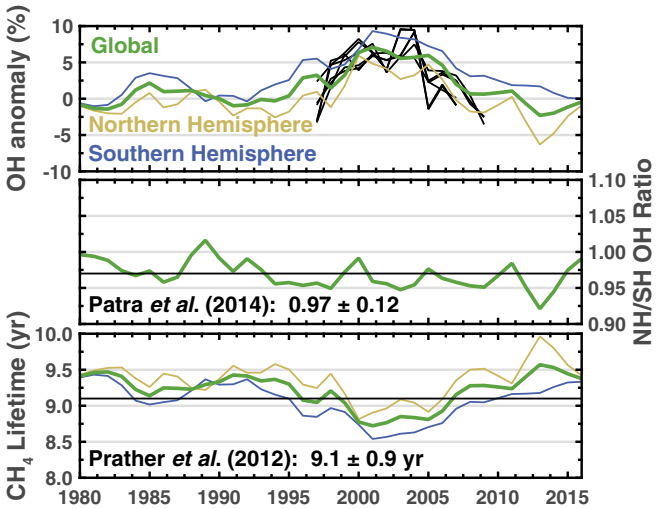

Fig. 3. Analysis of OH anomalies and the methane lifetime from the most likely solution. *Top* is the same as Fig. 2, *Bottom Right* but includes the OH anomalies from Montzka et al. (31), Rigby et al. (33), and McNorton et al. (21) (black lines). OH anomalies from Montzka et al. (31), Rigby et al. (33), and McNorton et al. (21) are offset such that their mean matches the mean 1997–2007 anomaly found here. *Middle* is the ratio of Northern to Southern Hemispheric OH and the black line is from Patra et al. (34). *Bottom* is the methane lifetime in our two-box model and the black line is the lifetime from Prather et al. (32). OH is the only sink included in our two-box model so the methane lifetime shown here is more representative of the actual methane lifetime, not a lifetime due to OH loss.

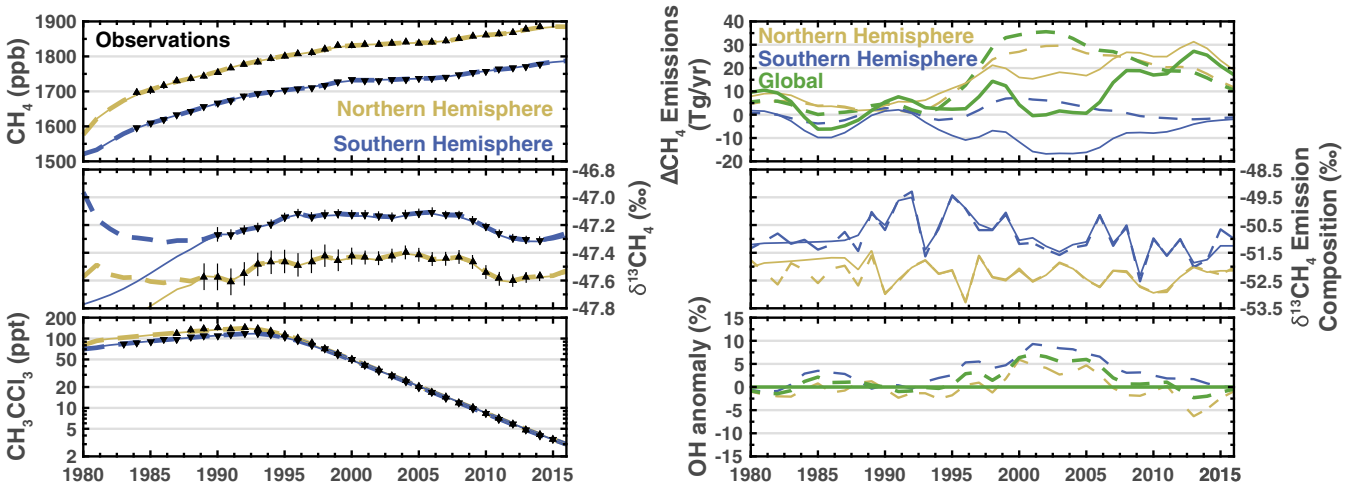

Fig. 4. Sensitivity test with fixed OH concentrations. Details are the same as in Fig. 2. Dashed lines are from the most likely solution (Fig. 2).

Hemispheric sources remains relatively stable during this period, indicating negligible changes in the proportion of emissions coming from isotopically light and heavy sources. Finally, the most likely solution found here suggests that the recent increase in atmospheric methane may be a transient feature driven by fluctuations in OH concentrations.

It is important to be cautious with source attribution based on isotope measurements. The isotopic composition of the Northern and Southern Hemispheric methane emissions remained largely unchanged in our three inversions (compare Figs. 2, *Middle Right*, 4, *Middle Right*, and 5, *Middle Right*) even though the spatiotemporal patterns in the methane emissions were radically different. As such, the interpretation of the sources driving the changes in methane emissions would differ. There is also a large overlap in the isotopic composition of different sources, further complicating the interpretation of the isotope measurements.

As for the methane stabilization, we find an ∼30-Tg/y increase in Northern Hemispheric methane emissions from 1992 to 2003 combined with an increasing OH anomaly is the most likely explanation for the methane trends from the early 1990s through the early 2000s; this generally agrees with the recent findings from McNorton et al. (21) who find that changes in OH can explain most of the methane stabilization. Based on our analysis, this seems more likely than previous work that has argued for the collapse of the former Soviet Union as a cause of the methane stabilization in the early 2000s (3, 8, 12, 16). However, we stress that our study relates only to aggregated (hemispheric-scale) drivers of the methane growth rate and does not preclude large subhemispheric-scale changes.

We performed two sensitivity tests where different potential drivers of decadal trends were held constant in the inversion. These sensitivity tests yielded two important conclusions: (*i*) Multiple (fundamentally different) scenarios can explain the observations and (*ii*) previous work that did not jointly estimate methane and OH aliased errors from one species to another.

For the former conclusion, both sensitivity tests are able to simulate the observations to within the observational uncertainties and the main difference between their likelihoods is due to the specification of the prior and assumptions in the analysis. As for the latter, previous work has rarely jointly estimated all parameters (e.g., methane emissions and OH concentrations) and is predisposed to a subset of solutions. For example, Schaefer et al. (16) derive a step increase of 19.7 Tg/y in methane emissions starting in 2007 and then attempt to explain the cause with isotope measurements. Their result is similar to our sensitivity test with fixed OH concentrations (Fig. 4) where we find an ∼20-Tg/y increase in methane emissions starting in 2007. However, this solution is not the most likely one if we allow OH concentrations to vary. A similar argument can be made against using fixed methane emissions when estimating global mean OH concentrations.

The methane stabilization and renewed growth can be reconciled through small changes to the sources and sinks (on the order of a few percent, relative to their global budgets). As such, small changes in the sources and sinks can have important implications for the observed atmospheric concentrations and make quantitative determination of the causes a difficult task. We find here that global methane emissions and OH likely changed by ±7% over 36 y but multiple scenarios can explain the observed changes in atmospheric methane, $\delta^{13}CH_4$, and methyl chloroform. As such, the apparent disagreement between past works on the causes of decadal trends in atmospheric methane (3–22) is, almost certainly, due to the problem being underdetermined.

Moving forward, stronger conclusions on the causes of decadal trends in atmospheric methane and OH could be drawn if we had other independent proxies for OH. Alternatively, a mechanistic explanation with supporting evidence for the potential changes in OH concentrations could allow us to draw stronger

Table 1. Prior distributions for components of the state vector

Model input	Distribution	a	b	μ	σ	τ, y
Annual components (emissions, isotopic compositions, and anomalies)						
NH CH_4, Tg/y	$\mathcal{N}_B$	300	500	412.5	20	5
SH CH_4, Tg/y	$\mathcal{N}_B$	100	250	137.5	20	5
NH $\delta^{13}CH_4$, ‰	$\mathcal{U}$	−60.0	−45.0	—	—	—
SH $\delta^{13}CH_4$, ‰	$\mathcal{U}$	−60.0	−45.0	—	—	—
NH MCF, Gg/y	$\mathcal{N}_B$	−1.0	β	α	γ	3
SH MCF, Gg/y	$\mathcal{U}$	−1.0	1.0	—	—	—
NH OH, %	$\mathcal{N}_B$	−20	20	0	10	3
SH OH, %	$\mathcal{N}_B$	−20	20	0	10	3
Initial conditions (IC)						
NH CH_4, ppb	$\mathcal{U}$	1,540	1,620	—	—	—
SH CH_4, ppb	$\mathcal{U}$	1,480	1,580	—	—	—
NH $\delta^{13}CH_4$, ‰	$\mathcal{U}$	−48.2	−46.6	—	—	—
SH $\delta^{13}CH_4$, ‰	$\mathcal{U}$	−48.2	−46.6	—	—	—
NH MCF, ppt	$\mathcal{U}$	15	135	—	—	—
SH MCF, ppt	$\mathcal{U}$	15	135	—	—	—

α is the updated annual MCF emissions from Prinn et al. (39), $\beta = \max([1.0\,\text{Gg/y}, 2\alpha])$, and $\gamma = \max([0.2\alpha, 1.5\,\text{Gg/y}])$. ppb, parts per billion; ppt, parts per trillion.

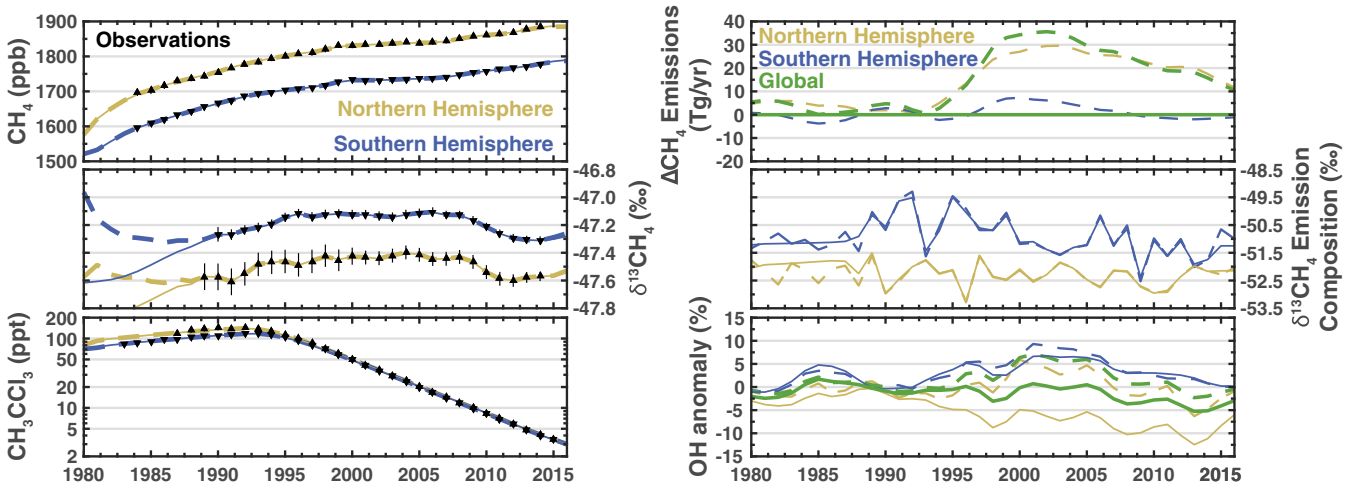

Fig. 5. Sensitivity test with fixed methane emissions. Details are the same as in Fig. 2. Dashed lines are from the most likely solution (Fig. 2).

conclusions. For example, changes in J (O^1D) due to stratospheric ozone could provide a large enough change in OH (37) but the changes in stratospheric ozone are only weakly correlated with the OH anomalies derived here (*SI Appendix*, section 5). Future work could also focus on obtaining higher spatially resolved constraints where the methane-to-ethane ratios and isotopic signatures of the sources are better constrained. This would also allow the use of more gradient information as could be discerned from satellite observations (15). More work is needed to discern the causes of decadal trends in atmospheric methane and OH.

Materials and Methods

The model and data used are available at https://github.com/alexjturner/BoxModel_PNAS_20161223.

Observational Records Used. All datasets used are publicly available. Methane observations are from National Oceanic and Atmospheric Administration's Earth System Research Laboratory (NOAA/ESRL). $\delta^{13}CH_4$ observations are from NOAA/ESRL; University of Washington, Seattle; University of Heidelberg, Heidelberg; and University of California, Irvine, CA. Methyl chloroform observations are from NOAA/ESRL and the Global Atmospheric Gases Experiment (GAGE)/Advanced GAGE (AGAGE) network. See *SI Appendix*, section 2 for more information on the observations.

Bootstrapping Hemispheric Averages and Uncertainties. We construct a hemispheric average atmospheric methane, $\delta^{13}CH_4$, and methyl chloroform via bootstrapping from the different observational records. The observational records are deseasonalized with a site-specific stable seasonal filter and we require that each observational record has at least a 5 y of data. We then generate a hemispherically averaged observational record and uncertainty by randomly drawing n observational records from the population of possible records, where n is the total number of observational records for that hemisphere. These n records are then combined using a block-averaging scheme with a 1-y window. This process is repeated 50 times. We then compute the mean and uncertainty from the 50 different time series. We also impose minimum uncertainty of 2 ppb and 0.03‰ for methane and $\delta^{13}CH_4$, respectively. Finally, we require that the uncertainty for older observations is greater than that for newer observations. See *SI Appendix*, section 2 for more information on the methodology.

Two-Box Model. We use a two-box model with three species: $^{12}CH_4$, $^{13}CH_4$, and MCF. The model simulates annual hemispheric concentrations for each species and considers loss, through reaction with OH, and interhemispheric transport with a timescale of 1 y: $\tau_{NS} = 1$ y (shown schematically in Fig. 1).

This gives us a set of six coupled ordinary differential equations:

$$\frac{\partial [X]_N(t)}{\partial t} = E_{X,N}(t) - k_{[X]}[\mathrm{OH}]_N(t)[X]_N(t) + \frac{[X]_S(t) - [X]_N(t)}{\tau_{NS}}$$

$$\frac{\partial [X]_S(t)}{\partial t} = E_{X,S}(t) - k_{[X]}[\mathrm{OH}]_S(t)[X]_S(t) + \frac{[X]_N(t) - [X]_S(t)}{\tau_{NS}},$$

where $[X](t)$ and $E_X(t)$ are the hemispheric concentrations and emissions, respectively, for a given species. N and S subscripts denote Northern and Southern Hemispheres. We do not consider other minor loss terms for methane [e.g., methanotrophic bacteria in aerated soils, chlorine and atomic oxygen radicals in the stratosphere, or reactions with chlorine radicals from sea salt in the marine boundary layer (13)] or methyl chloroform [e.g., uptake by the ocean (38)]. Lifetimes and reaction rate constants ($k_{[X]}$) used here should be viewed as total atmospheric lifetimes, not the lifetime with respect to OH loss. OH is plotted as an anomaly relative to a global mean concentration of 1×10^6 molec/cm^3.

Nonlinear, Stochastic, Bayesian Inversion. The two-box model (**F**) can be used to relate a state vector (**x**) to the observations (**y**),

$$\mathbf{y} = \mathbf{F}(\mathbf{x}) + \epsilon,$$

but there will always be some error (ϵ) associated with the both the observations and the model. The state vector in our work is the annual hemispheric MCF emissions, OH anomalies, methane emissions, and their isotopic composition, as well as the initial conditions for methane, $\delta^{13}CH_4$, and MCF. We can estimate the terms in this state vector using Bayesian inference,

$$P(\mathbf{x}|\mathbf{y}) \propto P(\mathbf{y}|\mathbf{x}) \cdot P(\mathbf{x}),$$

where $P(\mathbf{x}|\mathbf{y})$ is the posterior distribution, $P(\mathbf{y}|\mathbf{x})$ is the likelihood distribution, and $P(\mathbf{x})$ is the prior distribution. The two-box model is nonlinear due to the interaction between OH and methane: $k_{[CH_4]}[\mathrm{OH}](t)[CH_4](t)$. As such, we have adopted a stochastic method to infer the most likely solution.

We use the covariance matrix adaptation evolution strategy (CMA-ES) [Hansen (40) and references therein] to find the most likely solution. Typical sampling methods [such as Markov chain Monte Carlo (MCMC)] become prohibitively slow as the dimension of the state vector becomes large because they have trouble defining the proposal distribution. CMA-ES is an evolutionary algorithm that modifies the covariance matrix of the proposal distribution based on the fitness of multiple candidate solutions in a given generation. This allows CMA-ES to efficiently sample the posterior distribution. We restart CMA-ES with 10 different initializations and covariance matrices in an attempt to find a global minimum. In total, we draw 500,000,000 samples from the posterior distribution.

We assume the likelihood distribution is Gaussian with a diagonal covariance matrix populated by the uncertainties from the bootstrapping process. Because we are using a stochastic method, we can use non-Gaussian distributions that may be less restrictive and allow more flexible specification of the prior distribution. Our prior distribution is a convolution of uniform distributions: $\mathcal{U}(\mathbf{a}, \mathbf{b})$ and bounded normal distributions (which can be written as the product of a normal distribution and a uniform distribution): $\mathcal{N}_B(\mathbf{a}, \mathbf{b}, \boldsymbol{\mu}, \boldsymbol{\sigma}, \tau) = \mathcal{U}(\mathbf{a}, \mathbf{b}) \cdot \mathcal{N}(\boldsymbol{\mu}, \Sigma(\boldsymbol{\sigma}, \tau))$, where **a** is the lower bound, **b** is the upper bound, $\boldsymbol{\mu}$ is the mean, Σ is the covariance matrix, $\boldsymbol{\sigma}$ is the square root of the diagonal of Σ, and τ is the temporal correlation length scale for Σ. The prior distributions for each component of the state vector are shown in Table 1.

Linear, Gaussian, Bayesian Inversion for Sensitivity Tests. The two-box model is nonlinear because of the interaction between OH and methane, as mentioned above. However, the model becomes linear if we assume that either methane or OH is fixed. As such, our sensitivity tests (presented in Figs. 4 and 5) have a linear response. For computational efficiency, we assume Gaussian errors in the sensitivity tests to obtain a closed-form solution for the posterior distribution [for example, Rodgers (41)],

$$\hat{\mathbf{x}} = \left(\mathbf{S_a}^{-1} + \mathbf{K}^T\mathbf{S_o}^{-1}\mathbf{K}\right)^{-1}\mathbf{K}^T\mathbf{S_o}^{-1}(\mathbf{y} - \mathbf{K}\mathbf{x}),$$

where $\hat{\mathbf{x}}$ is the maximum a posteriori solution, $\mathbf{S_a}$ is the prior error covariance matrix, $\mathbf{K}$ is the Jacobian matrix of the two-box model, and $\mathbf{S_o}$ is the observational error covariance matrix.

ACKNOWLEDGMENTS. We thank E. Dlugokencky for providing methane data; S. Montzka, R. Prinn, S. O'Doherty, and R. Weiss for providing MCF data; and I. Levin, C. Veidt, B. Vaughn, J. White, and S. Englund for providing $\delta^{13}CH_4$ data. This work was supported by a Department of Energy Computational Science Graduate Fellowship (to A.J.T.) and by a NASA Carbon Monitoring System grant (to D.J.J.).

1. IPCC (2013) Climate change 2013: The physical science basis. *Contribution of Working Group I to the Fifth Assessment Report of the Intergovernmental Panel on Climate Change*, eds Stocker TF, Qin D, Plattner G-K, Tignor M, Allen SK, Boschung J, Nauels A, Xia Y, Bex V, Midgley PM (Cambridge Univ Press, Cambridge, UK).
2. Etheridge DM, Pearman GI, Fraser PJ (1992) Changes in tropospheric methane between 1841 and 1978 from a high accumulation-rate antarctic ice core. *Tellus Ser B Chem Phys Meteorol* 44:282–294.
3. Dlugokencky EJ (2003) Atmospheric methane levels off: Temporary pause or a new steady-state? *Geophys Res Lett* 30:1992.
4. Rigby M, et al. (2008) Renewed growth of atmospheric methane. *Geophys Res Lett* 35:L22805.
5. Dlugokencky EJ, et al. (2009) Observational constraints on recent increases in the atmospheric CH_4 burden. *Geophys Res Lett* 36:L18803.
6. Wang JS, et al. (2004) A 3-D model analysis of the slowdown and interannual variability in the methane growth rate from 1988 to 1997. *Global Biogeochem Cycles* 18:GB3011.
7. Fiore AM, Horowitz LW, Dlugokencky EJ, West JJ (2006) Impact of meteorology and emissions on methane trends, 1990–2004. *Geophys Res Lett* 33:L12809.
8. Aydin M, et al. (2011) Recent decreases in fossil-fuel emissions of ethane and methane derived from firn air. *Nature* 476:198–201.
9. Kai FM, Tyler SC, Randerson JT, Blake DR (2011) Reduced methane growth rate explained by decreased northern hemisphere microbial sources. *Nature* 476:194–197.
10. Bousquet P, et al. (2011) Source attribution of the changes in atmospheric methane for 2006–2008. *Atmos Chem Phys* 11:3689–3700.
11. Levin I, et al. (2012) No inter-hemispheric $\delta^{13}CH_4$ trend observed. *Nature* 486:E3–E4.
12. Simpson IJ, et al. (2012) Long-term decline of global atmospheric ethane concentrations and implications for methane. *Nature* 488:490–494.
13. Kirschke S, et al. (2013) Three decades of global methane sources and sinks. *Nat Geosci* 6:813–823.
14. Pison I, Ringeval B, Bousquet P, Prigent C, Papa F (2013) Stable atmospheric methane in the 2000s: Key-role of emissions from natural wetlands. *Atmos Chem Phys* 13:11609–11623.
15. Turner AJ, et al. (2016) A large increase in U.S. methane emissions over the past decade inferred from satellite data and surface observations. *Geophys Res Lett* 43:2218–2224.
16. Schaefer H, et al. (2016) A 21st-century shift from fossil-fuel to biogenic methane emissions indicated by $^{13}CH_4$. *Science* 352:80–84.
17. Hausmann P, Sussmann R, Smale D (2016) Contribution of oil and natural gas production to renewed increase in atmospheric methane (2007–2014): Top-down estimate from ethane and methane column observations. *Atmos Chem Phys* 16:3227–3244.
18. Franco B, et al. (2016) Evaluating ethane and methane emissions associated with the development of oil and natural gas extraction in North America. *Environ Res Lett* 11:044010.
19. Helmig D, et al. (2016) Reversal of global atmospheric ethane and propane trends largely due to us oil and natural gas production. *Nat Geosci* 9:490–495.
20. Dalsøren SB, et al. (2016) Atmospheric methane evolution the last 40 years. *Atmos Chem Phys* 16:3099–3126.
21. McNorton J, et al. (2016) Role of OH variability in the stalling of the global atmospheric CH_4 growth rate from 1999 to 2006. *Atmos Chem Phys* 16:7943–7956.
22. Rice AL, et al. (2016) Atmospheric methane isotopic record favors fossil sources flat in 1980s and 1990s with recent increase. *Proc Natl Acad Sci USA* 113:10791–10796.
23. Nisbet EG, et al. (2016) Rising atmospheric methane: 2007-2014 growth and isotopic shift. *Global Biogeochem Cycles* 30:1356–1370.
24. Schwietzke S, et al. (2016) Upward revision of global fossil fuel methane emissions based on isotope database. *Nature* 538:88–91.
25. Xiao Y, et al. (2008) Global budget of ethane and regional constraints on U.S. sources. *J Geophys Res* 113:D21306.
26. Kort EA, et al. (2016) Fugitive emissions from the Bakken shale illustrate role of shale production in global ethane shift. *Geophys Res Lett* 43:4617–4623.
27. Peischl J, et al. (2016) Quantifying atmospheric methane emissions from oil and natural gas production in the Bakken shale region of North Dakota. *J Geophys Res* 121:6101–6111.
28. Rice DD, Claypool GE (1981) Generation, accumulation, and resource potential of biogenic gas. *AAPG Bull* 65:5–25.
29. Martini AM, Budai JM, Walter LM, Schoell M (1996) Microbial generation of economic accumulations of methane within a shallow organic-rich shale. *Nature* 383:155–158.
30. Curtis JB (2002) Fractured shale-gas systems. *AAPG Bull* 86:1921–1938.
31. Montzka SA, et al. (2011) Small interannual variability of global atmospheric hydroxyl. *Science* 331:67–69.
32. Prather MJ, Holmes CD, Hsu J (2012) Reactive greenhouse gas scenarios: Systematic exploration of uncertainties and the role of atmospheric chemistry. *Geophys Res Lett* 39:L09803.
33. Rigby M, et al. (2013) Re-evaluation of the lifetimes of the major CFCs and CH_3CCl_3 using atmospheric trends. *Atmos Chem Phys* 13:2691–2702.
34. Patra PK, et al. (2014) Observational evidence for interhemispheric hydroxyl-radical parity. *Nature* 513:219–23.
35. Worden HM, et al. (2013) Decadal record of satellite carbon monoxide observations. *Atmos Chem Phys* 13:837–850.
36. Zeng G, et al. (2012) Trends and variations in CO, C_2H_6, and HCN in the Southern hemisphere point to the declining anthropogenic emissions of CO and C_2H_6. *Atmos Chem Phys* 12:7543–7555.
37. Holmes CD, Prather MJ, Søvde OA, Myhre G (2013) Future methane, hydroxyl, and their uncertainties: Key climate and emission parameters for future predictions. *Atmos Chem Phys* 13:285–302.
38. Wennberg PO, et al. (2004) Recent changes in the air-sea gas exchange of methyl chloroform. *Geophys Res Lett* 31:L16112.
39. Prinn RG, et al. (2000) A history of chemically and radiatively important gases in air deduced from ALE/GAGE/AGAGE. *J Geophys Res* 105:17751–17792.
40. Hansen N (2006) The CMA Evolution Strategy: A comparing review. *Towards a New Evolutionary Computation. Advances on Estimation of Distribution Algorithms*, eds Lozano JA, Larraaga P, Inza I, Bengoetxea E (Springer, Berlin), pp 75–102.
41. Rodgers CD (2000) *Inverse Methods for Atmospheric Sounding* (World Scientific, Singapore).

SI Appendix for "Ambiguity in the causes for decadal trends in atmospheric methane and hydroxyl"

Alexander J. Turner, Christian Frankenberg, Paul O. Wennberg, & Daniel J. Jacob

December 23, 2016

Contents

1 A criticism of the isotope analysis in Schaefer *et al.* (2016)

1.1 Abstract

Schaefer *et al.*[1] conclude that fossil-fuel methane sources did not cause the renewed growth in atmospheric methane because its isotopic signature ($\delta^{13}CH_4$) is too heavy. However, fossil-fuel sources are not strictly thermogenic in origin and past work has measured fossil-fuel sources with $\delta^{13}CH_4$ that could explain 0% to 100% of the renewed growth in atmospheric methane since 2007.

1.2 Comment

To understand the reasons for changes in atmospheric methane since the 1990s, Schaefer *et al.*[1] examined global trends in atmospheric methane and measurements of bulk carbon isotope ratios in atmospheric methane ($\delta^{13}CH_4$) from 17 sites. They use these 17 records to construct a globally averaged isotope ratio in atmospheric methane ($\delta^{13}CH_{4(atm)}$). Their data set shows a 0.5‰ increase in $\delta^{13}CH_{4(atm)}$ from 1980 to 1998, a constant $\delta^{13}CH_{4(atm)}$ of -47.2‰ from 1998 to 2008, and a 0.2‰ decrease in $\delta^{13}CH_{4(atm)}$ from 2008 to 2014. Schaefer *et al.*[1] posit that different sources and sinks have distinct isotopic signatures that can be used to determine the sources causing these changes in $\delta^{13}CH_{4(atm)}$. Specifically, Schaefer *et al.*[1] assume that pyrogenic, thermogenic, and biogenic methane sources have isotopic signatures of -22‰, -37‰, and -60‰, respectively.

Schaefer *et al.*[1] then create reconstructions of atmospheric methane concentrations and $\delta^{13}CH_{4(atm)}$ using emission perturbations from sources with different isotopic signatures. They find that a +19.7 Tg a^{-1} source with an average isotopic signature ($\delta^{13}CH_{4(so)}$) of -59‰ best explains the observed decrease in $\delta^{13}CH_{4(atm)}$ from 2008 to 2014. Based on this, they conclude that biogenic methane sources are responsible for the renewed growth because $\delta^{13}CH_{4(so)}$ matches their assumed isotopic signature for biogenic methane sources. A major conclusion from the abstract of Schaefer *et al.*[1] is: "*Thermogenic emissions didn't resume to cause the renewed [CH_4]-rise after 2006*" and from their conclusions: "*Importantly, they [fossil-fuel emissions] are a minor contributor to the renewed [CH_4]-rise.*"

Schaefer *et al.*[1] reach the latter conclusion because they assume that fossil-fuel sources emit thermogenic methane. However, fossil-fuel sources are not strictly thermogenic in origin. In fact, over 20% of the world's natural gas accumulations are of biogenic origin[2]. Biogenic gas is particularly common in non-conventional gas resources such as coalbed methane and organic shale gas basins[3]. Numerous US basins with non-conventional natural gas resources have been found to be predominately biogenic methane (e.g., the Antrim Shale[3, 4, 5], the New Albany Shale[4], and the Powder River Basin[6]).

As such, fossil-fuel and non-fossil methane sources have overlapping isotopic signatures. Table S1 lists measured methane isotope compositions for various sources compiled from previous work[7, 8, 6, 5, 9]. From Table S1, we find fossil-fuel methane isotope signatures ($\delta^{13}CH_{4(ff)}$) that range from -15‰ to -76‰ and non-fossil methane isotope signatures ($\delta^{13}CH_{4(nf)}$) that range from -31‰ to -93‰. Recently, Stolper *et al.*[5] found a $\delta^{13}CH_{4(ff)}$ of -58.0‰ to -60.4‰ for methane samples collected from boreholes in the Gulf of Mexico and Wang *et al.*[6] found a $\delta^{13}CH_{4(ff)}$ of -58.6‰ to -62.0‰ for methane sampled from multiple gas wells in the Powder River Basin. Both of these fossil-fuel methane sources have a $\delta^{13}CH_4$ that match the best-fit $\delta^{13}CH_{4(so)}$ from Schaefer *et al.*[1].

Table 1: Measured methane isotope compositions ($\delta^{13}CH_4$) for various sources.

Source[a]	$\delta^{13}CH_4$	Gas Type[b]	Reference
fossil-fuel (-15‰ to -76‰)			
Powder River Basin	-58.6‰ to -62.0‰	B	Wang *et al.*[6][c]
Gulf of Mexico	-58.0‰ to -60.4‰	B	Stolper *et al.*[5][d]
Antrim Shale	-50.2‰ to -53.2‰	M	Stolper *et al.*[5][d], Stolper *et al.*[10][e]
Potiguar Basin	-37.4‰ to -49.6‰	T	Stolper *et al.*[5][d]
Guyamas Basin	-44.0‰	T	Wang *et al.*[6][c]
Haynesville Shale	-35.2‰ to -38.9‰	T	Stolper *et al.*[5][d]
Marcellus Shale	-34.2‰ to -35.8‰	T	Stolper *et al.*[5][d]
North Appalachia Basin	-25.7‰ to -36.2‰	T	Wang *et al.*[6][c]
Coal-associated gas	-15‰ to -70‰	M	Bréas *et al.*[7][f]
Oil-associated gas	-30‰ to -60‰	M	Bréas *et al.*[7][f]
Gas drilling, pipeline leakage	-41‰ to -76‰	M	Bréas *et al.*[7][f]
Biomass Burning (C4 vegetation)	-17 ± 3‰	P	Dlugokencky *et al.*[8][g]
Biomass Burning (C3 vegetation)	-26 ± 3‰	P	Dlugokencky *et al.*[8][g]
Biomass Burning	-24‰ to -32‰	P	Bréas *et al.*[7][f]
non-fossil (-31‰ to -93‰)			
Hydrates (North Cascadia Margin)	-61.6‰ to -68.5‰	B	Wang *et al.*[6][c]
Pennsylvania Dairy Cows (C4 diet)	-52.8‰ to -54.2‰	B	Wang *et al.*[6][c]
Ruminants (C3 diet)	-61‰ to -76‰	B	Bréas *et al.*[7][f]
Ruminants (C4 diet)	-47‰ to -55‰	B	Bréas *et al.*[7][f]
Swamp (Massachusetts)	-59.2‰ to -59.7‰	B	Wang *et al.*[6][c]
Swamp (California)	-63.8‰ to -68.0‰	B	Wang *et al.*[6][c]
Lake (Massachusetts)	-65.5‰ to -71.0‰	B	Wang *et al.*[6][c]
Wetlands (Bogs)	-51‰ to -85‰	B	Bréas *et al.*[7][f]
Wetlands (Swamps)	-31‰ to -73‰	B	Bréas *et al.*[7][f]
Rice Paddies	-50‰ to -68‰	B	Bréas *et al.*[7][f]
Landfills	-52‰ to -63‰	B	Bréas *et al.*[7][f]
Termites	-44‰ to -93‰	B	Bréas *et al.*[7][f]
Isotope signatures assumed in Schaefer et al.[1]			
Pyrogenic	-22‰	P	Dlugokencky *et al.*[8], Bréas *et al.*[7]
Thermogenic	-37‰	T	Dlugokencky *et al.*[8], Bréas *et al.*[7]
Biogenic	-60‰	B	Dlugokencky *et al.*[8], Bréas *et al.*[7]

[a] We have included biomass burning in the "fossil-fuel" category, as Bréas *et al.*[7] did.
[b] "P" is pyrogenic, "T" is thermogenic, "B" is biogenic, and "M" is mixed biogenic and thermogenic.
[c] Table S1 in Wang *et al.*[6].
[d] Table S2 in Stolper *et al.*[5].
[e] Table 3 in Stolper *et al.*[10].
[f] Table 4 in Bréas *et al.*[7].
[g] Table 1 in Dlugokencky *et al.*[8].

We can use the isotope mass-balance to compute the fraction of emissions from fossil-fuel methane sources (f):

$$f = \frac{E_{(\mathrm{ff})}}{E_{(\mathrm{so})}} = \frac{\delta^{13}\mathrm{CH}_{4(\mathrm{so})} - \delta^{13}\mathrm{CH}_{4(\mathrm{nf})}}{\delta^{13}\mathrm{CH}_{4(\mathrm{ff})} - \delta^{13}\mathrm{CH}_{4(\mathrm{nf})}} \quad (1)$$

where $E_{(\mathrm{ff})}$ is the potential increase in fossil-fuel methane emissions and $E_{(\mathrm{so})}$ is the increased emissions required to explain the renewed increase in atmospheric methane, Schaefer *et al.*[1] find $E_{(\mathrm{so})} = +19.7$ Tg a^{-1}.

Fig. S1 shows the fraction of the renewed growth in atmospheric methane attributable to fossil-fuel sources over the plausible range of fossil-fuel and non-fossil methane isotope signatures from Table S1. Fig. 1 uses the best-fit $\delta^{13}\mathrm{CH}_{4(\mathrm{so})}$ of -59‰ from Schaefer *et al.*[1]. Not surprisingly, we find that a fossil-fuel or non-fossil methane source with a $\delta^{13}\mathrm{CH}_4$ of -59‰ could explain 100% of the observed changes in $\delta^{13}\mathrm{CH}_{4(\mathrm{atm})}$. However, there are also other plausible scenarios where fossil-fuel methane sources could explain between 0% and 100% of the observed changes in $\delta^{13}\mathrm{CH}_{4(\mathrm{atm})}$. For example, an increase in methane emissions that is 55% fossil-fuel and 45% non-fossil with isotope signatures of -50‰ and -70‰, respectively, could also explain the observed changes in $\delta^{13}\mathrm{CH}_{4(\mathrm{atm})}$.

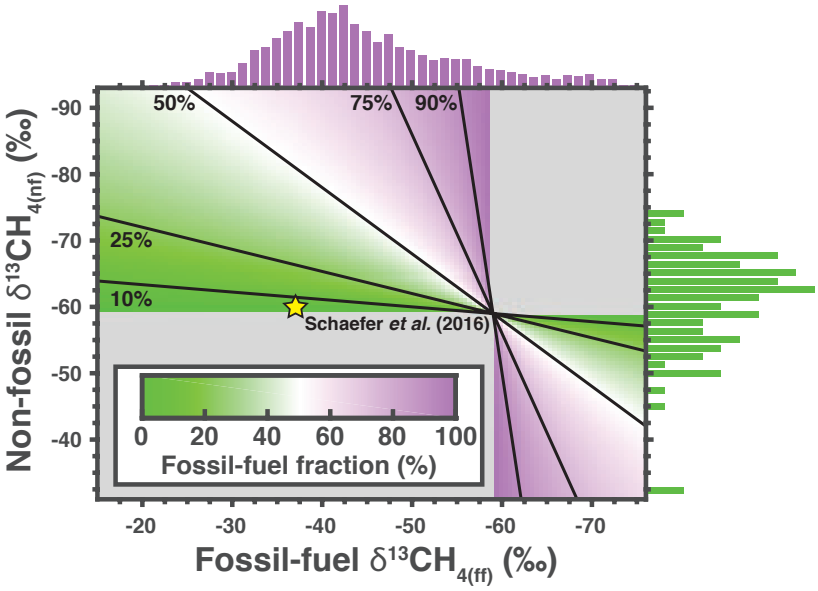

Figure 1: Fraction of renewed growth since 2007 in atmospheric methane attributable to fossil-fuel methane sources (f). Computed using Eq. 1 with a $\delta^{13}\mathrm{CH}_{4(\mathrm{so})}$ of -59‰, the best fit $\delta^{13}\mathrm{CH}_{4(\mathrm{so})}$ from Schaefer *et al.*[1]. The x- and y-axes span the range of $\delta^{13}\mathrm{CH}_4$ measured for fossil-fuel and non-fossil methane sources from Table S1. Pink (green) histogram is the distribution of fossil-fuel (non-fossil) isotopic signatures from Schwietzke *et al.*[11]. Gray areas indicate non-physical solutions. Yellow star is the assumed isotopic signatures from Schaefer *et al.*[1]: $\delta^{13}\mathrm{CH}_{4(\mathrm{nf})} = -60$‰ and $\delta^{13}\mathrm{CH}_{4(\mathrm{ff})} = -37$‰.

In contrast to Schaefer *et al.*[1], our analysis presented here demonstrates that an increase in fossil-fuel methane sources could be a major contributor to the renewed growth in atmospheric methane since 2007. Given the overlapping isotope signatures of fossil-fuel and non-fossil sources, future work should be cautious when interpreting changes in $\delta^{13}\mathrm{CH}_{4(\mathrm{atm})}$.

2 Additional information on the observations, hemispheric averages, and model

We use publicly available data from NOAA/ESRL, INSTAAR, U.C. Irvine, U. Washington, GAGE, and AGAGE. For methane observations, we use 92 monitoring stations from the NOAA/ESRL global monitoring network. For $\delta^{13}CH_4$ we use 32 monitoring sites from NOAA/ESRL/INSTAAR, U.C. Irvine, and U. Washington (see Table S2). For methyl chloroform we use 22 sites from NOAA/ESRL, GAGE, and AGAGE (see Table S2).

Fig. S2 shows the individual de-seasonalized observational records and the bootstrapped hemispheric averages with uncertainties. The process for obtaining the hemispheric averages and uncertainties is as follows:

1. De-seasonalize each observational record with a stable seasonal filter and a 1-year moving average.
2. Group each de-seasonalized observational record by hemisphere and determine the number of sites in the Northern (Southern) hemisphere: n_N (n_S).
3. Randomly select n_N (n_S) records from the Northern (Southern) hemisphere with replacement.
4. Compute the hemispheric average from the randomly selected n_N (n_S) records.
5. Repeat n_B times, yielding n_B different hemispheric averages.
6. Compute the mean hemispheric average and standard deviation from the n_B realizations.

We use a reaction rate for OH + CH_4 of 3.4×10^{-15} cm^3 $molec^{-1}$ s^{-1} (derived from the three-parameter expression: $k(T) = 2.80 \times 10^{-14} T^{0.667} \exp(-1575/T)$ from Burkholder *et al.*[12] using a temperature of 270 K) and a kinetic isotope effect (KIE) of 1.005 from Burkholder *et al.*[12] (originally from Cantrell *et al.*[13]: 1.005±0.002). Our simple 2-box model neglects minor methane sinks (methanotrophic bacteria in aerated soils, chlorine and atomic oxygen radicals in the stratosphere, and chlorine radicals from sea salt in the marine boundary layer) and only considers a single loss process for atmospheric methane: reaction with OH. As such, we could be aliasing errors from those minor loss pathways onto the estimated OH concentrations.

3 Other output from the main text inversions

This section presents additional output from the main text inversions. Specifically, we present the inter-hemispheric difference, the methyl chloroform emissions, and the residuals.

Fig. S3 shows the inter-hemispheric differences (IHD) of atmospheric methane and $\delta^{13}CH_4$ as well as the underlying drivers for the simulated IHD. We find that the posterior simulation is able to capture most of the IHD in in atmospheric methane and $\delta^{13}CH_4$. The most prominent feature in the IHD is the minimum from 1989 to 1993. In our posterior simulation, this minimum is due to a slight (∼7 Tg/yr) increase in Southern hemispheric methane emissions.

Fig. S4 shows the methyl chloroform emissions from the the main text inversions as well as the emissions from Prinn *et al.*[14], used as a prior. All three inversions find that the Prinn *et al.*[14] emissions are, generally, overestimated before 2000.

Table 2: Monitoring stations used for $\delta^{13}CH_4$ and methyl chloroform.

Station	Code	Latitude	Laboratory
isotope measurements			
Alert, Canada	ALT	82°N	NOAA/ESRL/INSTAAR
Ascension Island, UK	ASC	8°S	NOAA/ESRL/INSTAAR
Terceira Island, Azores	AZR	39°N	NOAA/ESRL/INSTAAR
Baring Head, NZ	BHD	41°S	NOAA/ESRL/INSTAAR
Barrow, USA	BRW	71°N	NOAA/ESRL/INSTAAR
Cold Bay, USA	CBA	55°N	NOAA/ESRL/INSTAAR
Cape Grim, Australia	CGO	41°S	NOAA/ESRL/INSTAAR
Cape Kumukahi, USA	KUM	20°N	NOAA/ESRL/INSTAAR
Lac La Biche, Canada	LLB	55°N	NOAA/ESRL/INSTAAR
High Altitude Global Climate Observation Center, Mexico	MEX	19°N	NOAA/ESRL/INSTAAR
Mace Head, Ireland	MHD	53°N	NOAA/ESRL/INSTAAR
Mauna Loa, USA	MLO	20°N	NOAA/ESRL/INSTAAR
Niwot Ridge, USA	NWR	40°N	NOAA/ESRL/INSTAAR
Cape Matatula, Samoa	SMO	14°S	NOAA/ESRL/INSTAAR
South Pole, Antarctica	SPO	90°S	NOAA/ESRL/INSTAAR
Summit, Greenland	SUM	73°N	NOAA/ESRL/INSTAAR
Tae-ahn Peninsula, Korea	TAP	37°N	NOAA/ESRL/INSTAAR
Mt. Waliguan, China	WLG	36°N	NOAA/ESRL/INSTAAR
Ny-Alesund, Norway	ZEP	80°N	NOAA/ESRL/INSTAAR
Alert, Canada	ALT	82°N	U. Heidelberg
Izana, Portugal	IZA	28°N	U. Heidelberg
Neumayer, Antarctica	NEU	71°S	U. Heidelberg
Niwot Ridge, USA	NWR	41°N	U.C. Irvine
Montana de Oro, USA	MDO	35°N	U.C. Irvine
Cape Grim, Australia	CGO	41°S	U. Washington
Olympic Peninsula, USA	OPW	48°N	U. Washington
Fraserdale, Canada	FSD	50°N	U. Washington
Majuro, Marshall Islands	MMI	7°N	U. Washington
Mauna Loa, USA	MLO	19°N	U. Washington
Baring Head, NZ	BHD	41°S	U. Washington
Barrow, USA	BRW	71°N	U. Washington
Tutuila, Samoa	SMO	14°S	U. Washington
methyl chloroform measurements			
Alert, Canada	ALT	82°N	NOAA/ESRL
Barrow, USA	BRW	71°N	NOAA/ESRL
Cape Grim, Australia	CGO	41°S	NOAA/ESRL
Cape Kumukahi, USA	KUM	20°N	NOAA/ESRL
Mace Head, Ireland	MHD	53°N	NOAA/ESRL
Mauna Loa, USA	MLO	20°N	NOAA/ESRL
Palmer Station, Antarctica	PSA	65°S	NOAA/ESRL
Niwot Ridge, USA	NWR	40°N	NOAA/ESRL
Cape Matatula, Samoa	SMO	14°S	NOAA/ESRL
South Pole, Antarctica	SPO	90°S	NOAA/ESRL
Summit, Greenland	SUM	73°N	NOAA/ESRL
Trinidad Head, USA	THD	41°N	NOAA/ESRL
Cape Grim, Australia	CGO	41°S	GAGE
Mace Head, Ireland	MHD	53°N	GAGE
Cape Meares, USA	ORG	45°N	GAGE
Ragged Point Barbados	RPB	13°N	GAGE
Cape Matatula, Samoa	SMO	14°S	GAGE
Cape Grim, Australia	CGO	41°S	AGAGE
Mace Head, Ireland	MHD	53°N	AGAGE
Ragged Point Barbados	RPB	13°N	AGAGE
Cape Matatula, Samoa	SMO	14°S	AGAGE
Trinidad Head, USA	THD	41°N	AGAGE

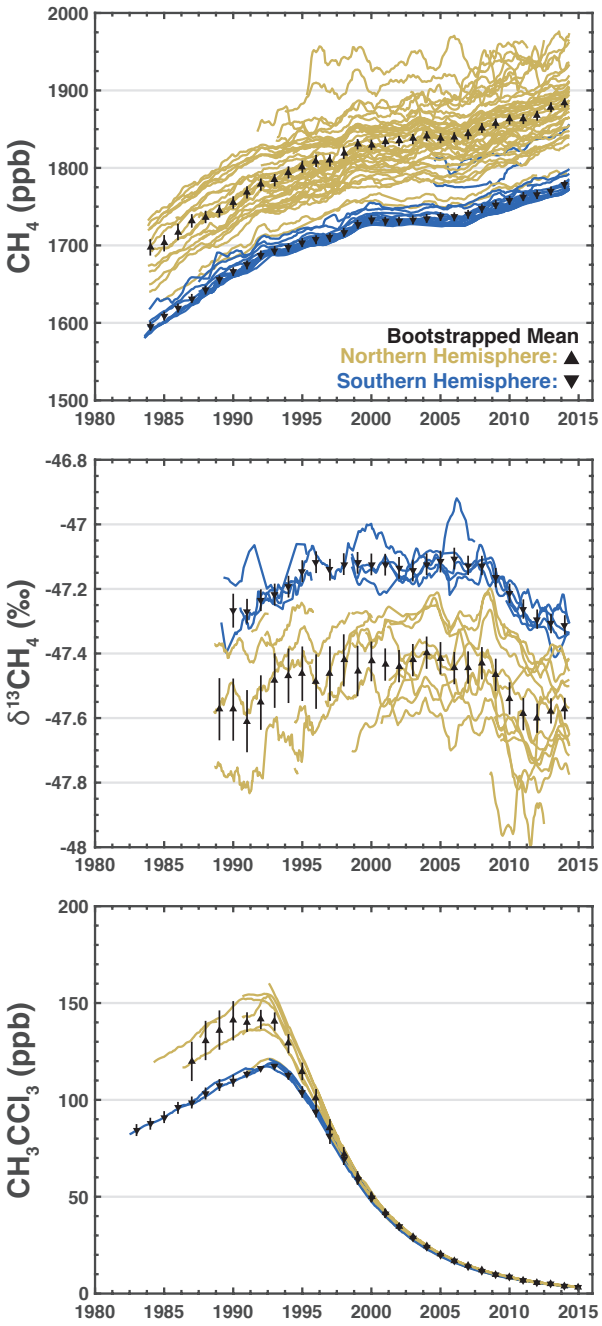

Figure 2: Bootstrapped hemispheric averages and uncertainties. Each line is the de-seasonalized time-series from a single site colored by hemisphere (Northern hemisphere is yellow and Southern hemisphere is blue). The black triangles are the annual hemispheric means and the error bars are the uncertainty derived from the bootstrapping. Top panel is the methane observations, middle panel is the $\delta^{13}CH_4$ observations, and the bottom panel is the methyl chloroform observations.

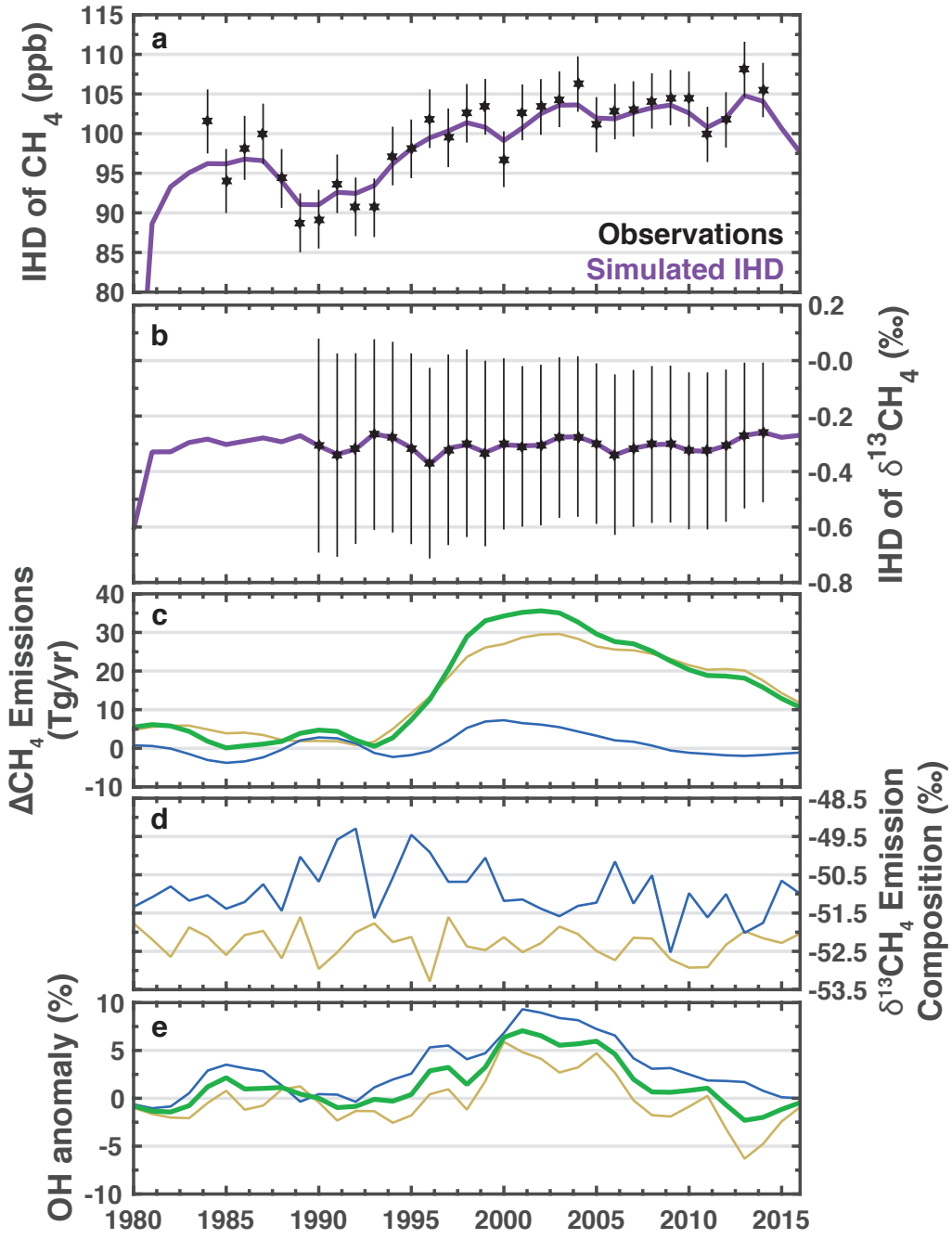

Figure 3: Inter-hemispheric difference (IHD) of atmospheric methane and $\delta^{13}CH_4$. (**a**) Inter-hemispheric difference of atmospheric methane. Black stars are the observed IHD and solid purple line is the simulated IHD using the most likely solution from the non-linear inversion. (**b**) Inter-hemispheric difference of $\delta^{13}CH_4$ in atmospheric methane. (**c**–**e**) Same as right column from main text Fig. 2. Drivers of the decadal trends in atmospheric methane. Green line is the global value, yellow line is the Northern hemisphere, and blue line is the Southern hemisphere.

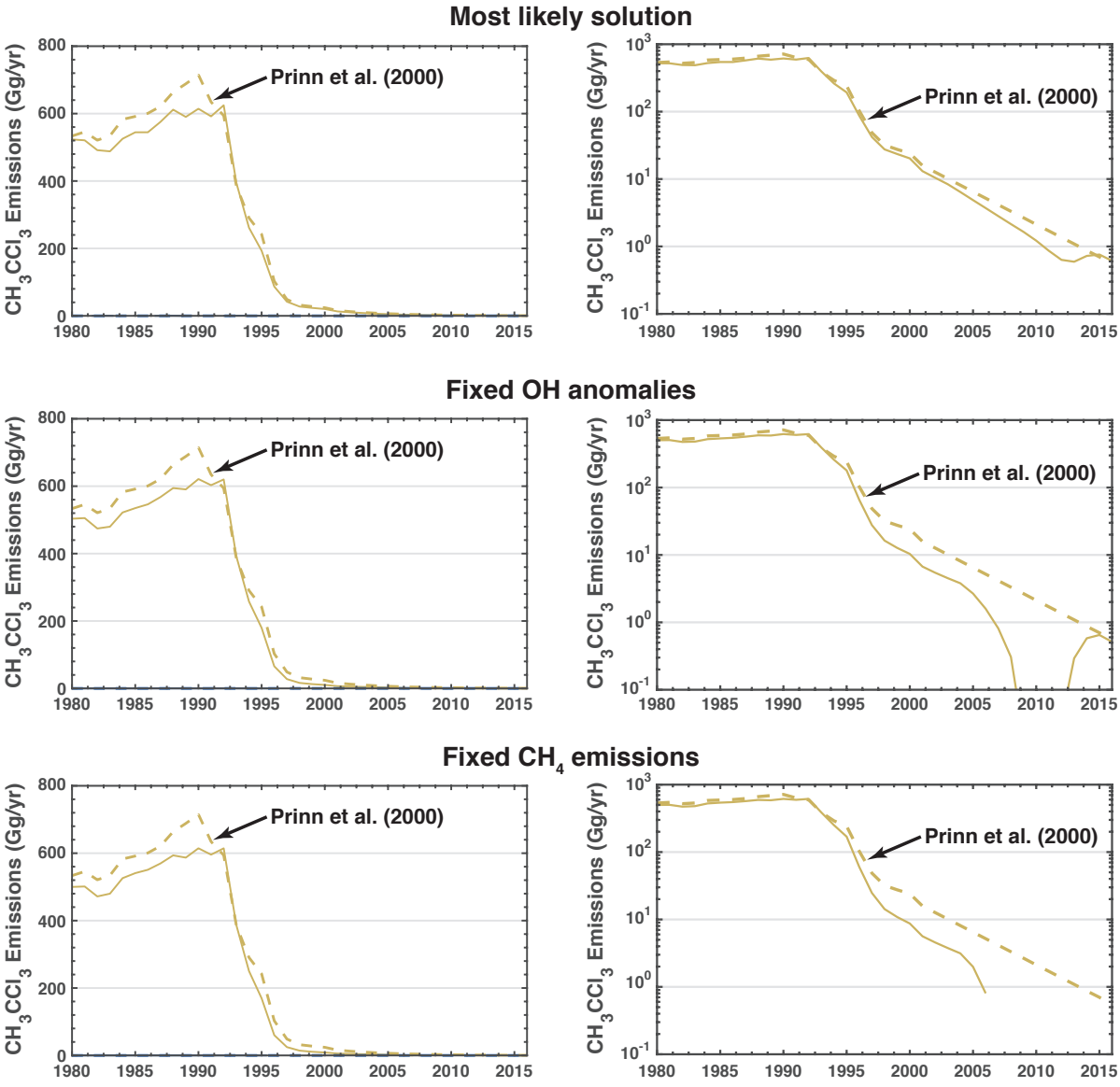

Figure 4: Methyl chloroform emissions. Top row shows the emissions from the most likely solution, middle row shows the fixed OH case, and bottom row shows the fixed methane emissions case. Left column is a linear scale and right column is a log scale. Dashed line in all panels is the Prinn *et al.*[14] emissions used as a prior for the inversions. Note that the posterior solution does allow for negative emissions (uptake by the oceans) and are not shown in the log-scale column.

Figs. S5, S6, and S7 show the residuals from the most likely solution, the fixed OH case, and the fixed methane emissions case, respectively. We can see that in all cases the uncertainty in the residuals bounds zero. However, we do find a systematic overestimate in the methyl chloroform observations before 2000. This overestimate is due to three factors: (1) using a Gaussian (or Gaussian-like) prior in the inversions, the (2) the methyl chloroform are overestimated before 2000, and (3) the large uncertainty in the early methyl chloroform observations. These three factors lead to a systematic overestimate in the methyl chloroform observations prior to 2000. Although as mentioned before, the uncertainty in the overestimate bounds zero.

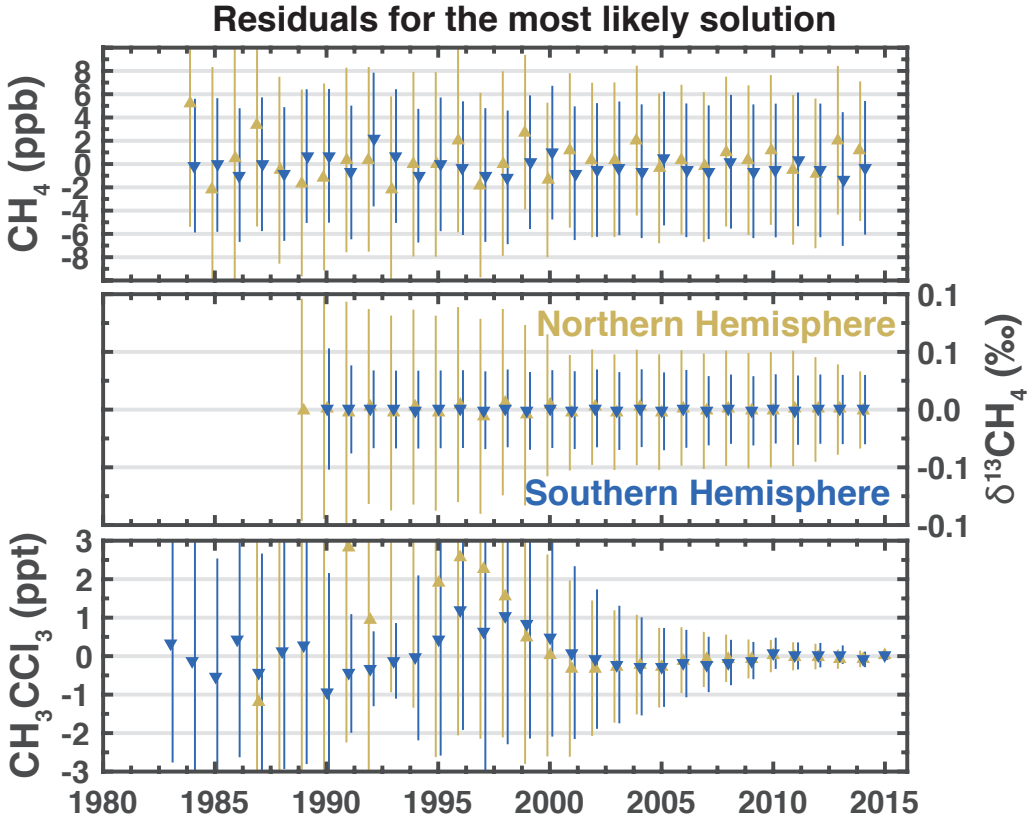

Figure 5: Residuals for the most likely solution. Top panel shows the residuals for the methane observations, middle planel is the $\delta^{13}CH_4$ observations, and bottom panel is the methyl chloroform observations. Yellow is the Northern hemisphere and blue is the southern hemisphere.

4 Additional sensitivity tests

This section presents additional sensitivity tests. All the additional sensitivity tests were done using a simple linear Gaussian inversion. Overall, we find that the magnitude of the drivers is sensitive to the assumed uncertainty but the temporal patterns are, reasonably, robust.

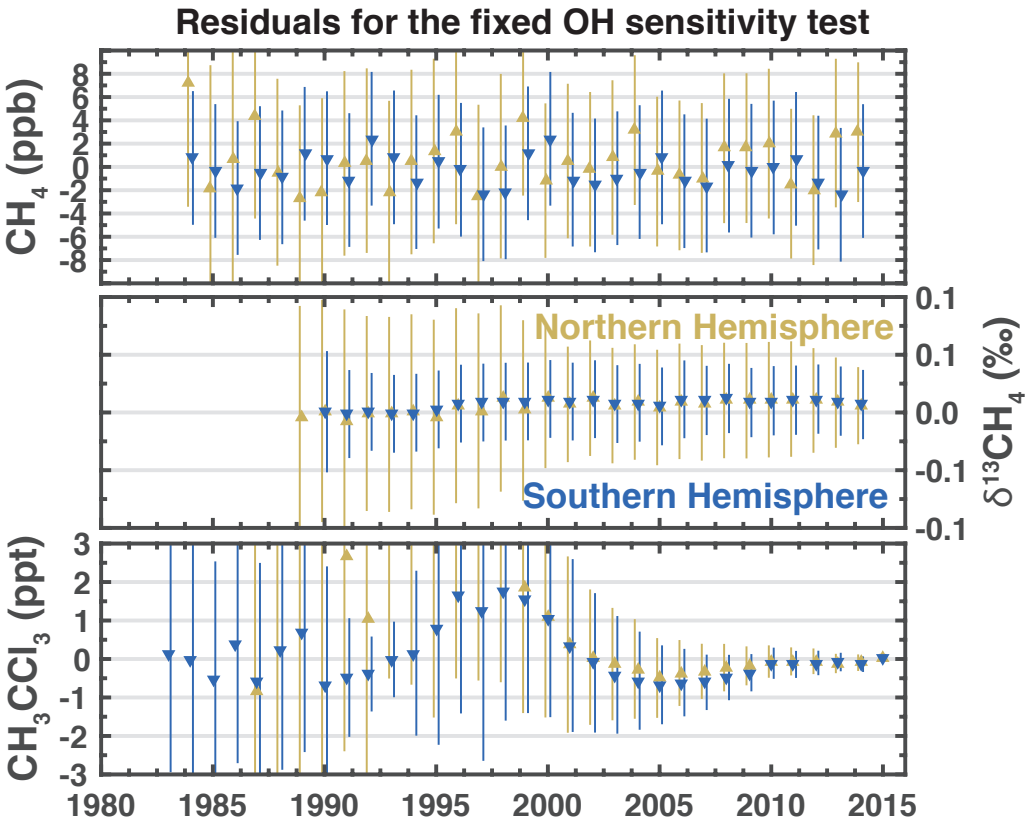

Figure 6: Same as Fig. S6 but for the sensitivity test with fixed OH (main text Fig. 4).

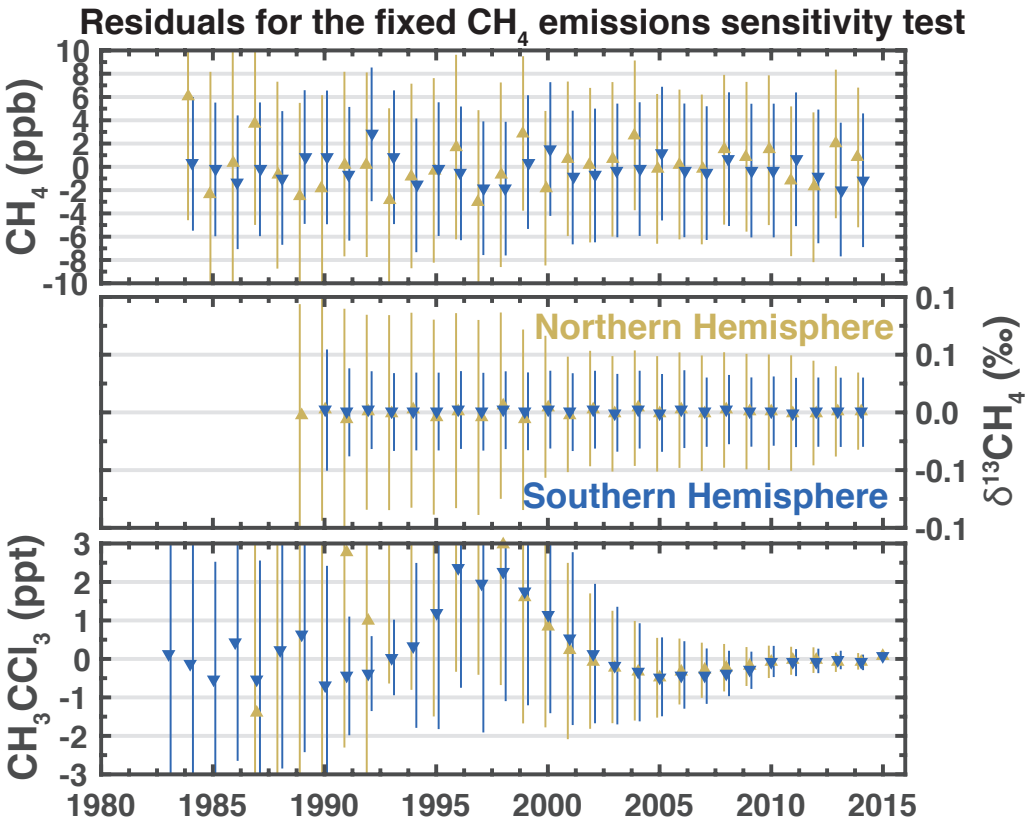

Figure 7: Same as Fig. S7 but for the sensitivity test with fixed methane emissions (main text Fig. 5).

4.1 Varying the prior uncertainties

We performed additional inversions where the uncertainty in the methane emissions was varied (Fig. S8) and the uncertainty in the OH anomalies was varied (Fig. S9). Overall, we find that the magnitude of the drivers is sensitive to the assumed uncertainty but the temporal patterns are (reasonably) robust.

4.2 Alternate hemispheric averages

We tested the sensitivity to the hemispheric averaging scheme by using an alternate set of hemispheric averages. The CH_4 and $\delta^{13}CH_4$ averages were provided by E. Dlugokencky (E. Dlugokencky, NOAA/ESRL, personal communication; data included in tarball with code) and the methyl chloroform averages were from NOAA/ESRL (see the "`combined/HATS_global_MC.txt`" file). The alternate hemispheric averages for CH_4 and $\delta^{13}CH_4$ did not report an uncertainty, so we assume the same uncertainty as the bootstrapping method presented in Section 2. Fig. S10 shows the resulting hemispheric averages from the two schemes.

The overall spatial and temporal patterns for the methane emissions and OH anomalies are largely unaffected (see Fig. S11). The only major difference is in the resulting $\delta^{13}CH_4$ emission composition

4.3 Varying the methyl chloroform parameters

The methyl chloroform residuals have a potential systematic difference between 1995 and 2000 (see Figs. S5, 6, and 7). In all cases the uncertainty on the residuals bound zero. Additionally, our most likely solution has the smallest residual during this period. Nevertheless, we investigate the potential impact of this systematic residual.

We performed two sensitivity tests to look at the impact of the residual:

1. Limit the uncertainty in methyl chloroform observations to 2 ppt.
2. Smooth the methyl chloroform emissions from Prinn *et al.*[14] with a 5-year filter.
3. Limit the uncertainty and smooth the methyl chloroform emissions.

Fig. S12 shows the original methyl chloroform emissions and the smoothed emissions. Fig. S13 shows the main drivers from three cases we investigated as well as the residuals. The conclusions from the work are, largely, unaffected by the treatment of methyl chloroform emissions in the early part of the record.

Case #1 and #3 result in larger changes in OH and methane emissions in the late 1980s and early 1990s. This is because the uncertainty in the observations is reduced, resulting in the observations carrying more weight. Case #2 does not result in qualitatively different drivers (Fig. S12).

4.4 Varying the interhemispheric exchange time

We performed additional inversions where we varied the interhemispheric exchange time (τ). Fig. S14. Overall, we find that the magnitude of the drivers is sensitive to the assumed uncertainty but the temporal patterns are (reasonably) robust.

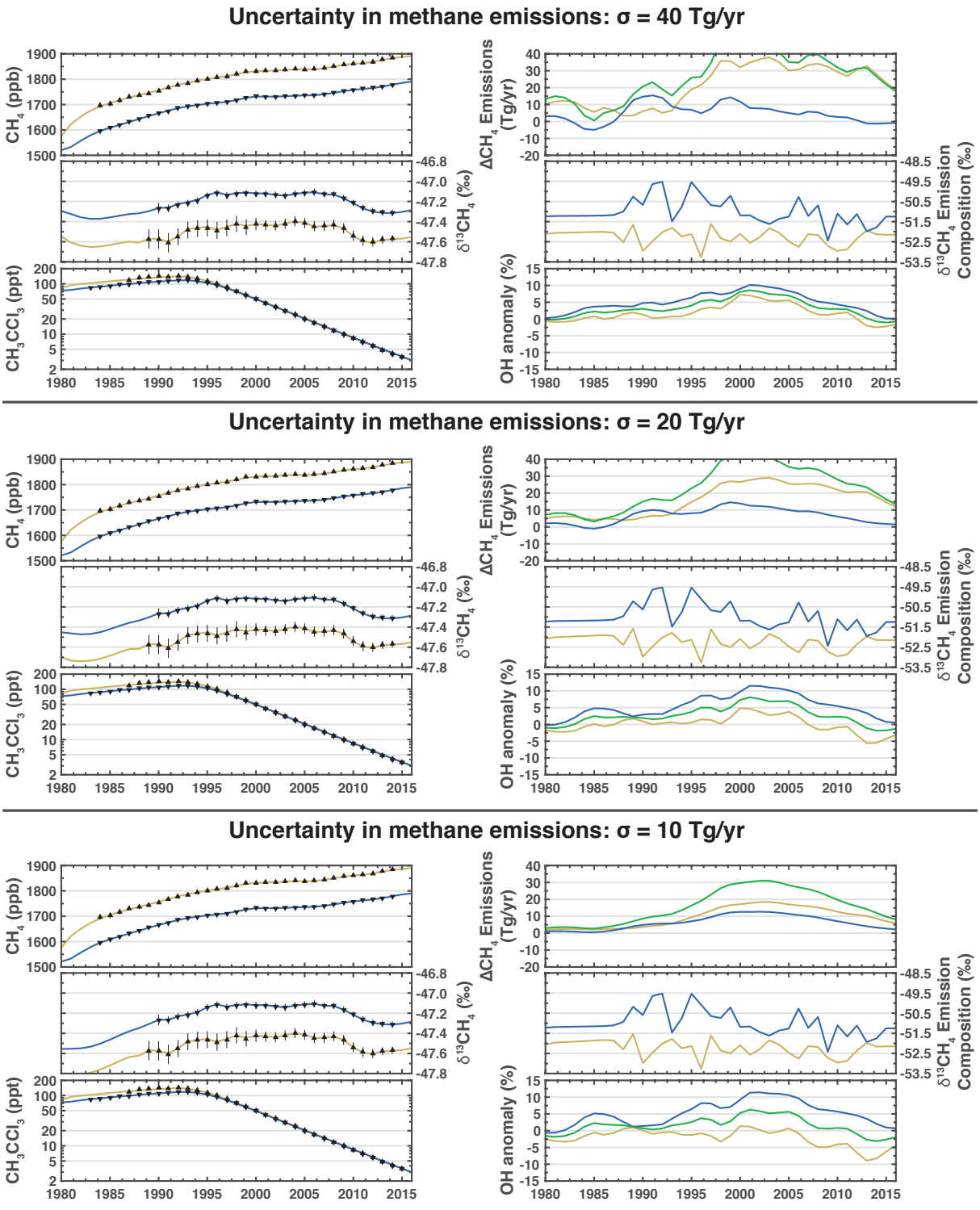

Figure 8: Varying the prior uncertainties in methane emissions. Each row is the same as main text Fig. 2 but using a linear Gaussian inversion with varying uncertainty in the methane emissions. Top row uses an uncertainty of 40 Tg/yr, middle row uses 20 Tg/yr, and bottom row uses 10 Tg/yr.

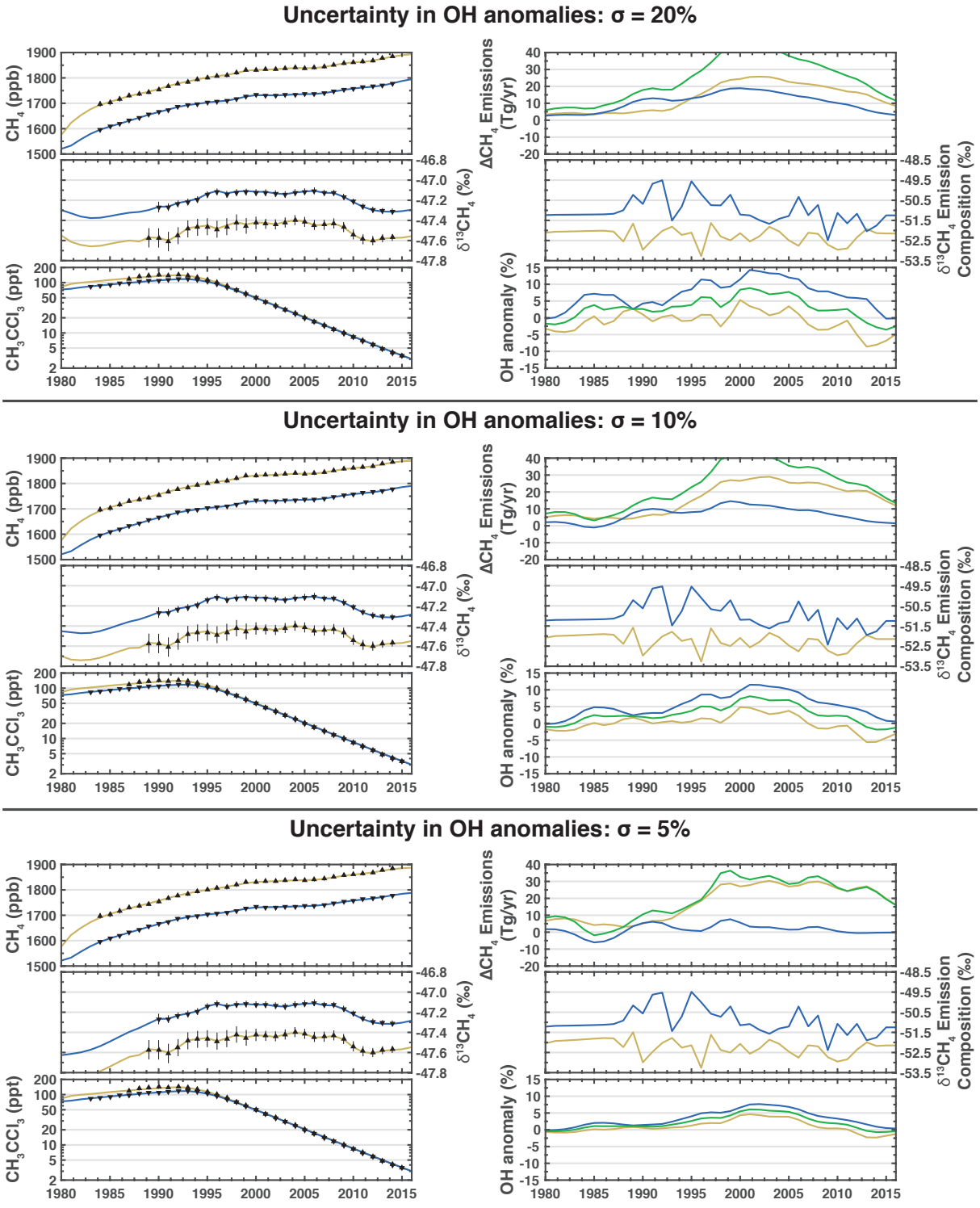

Figure 9: Varying the prior uncertainties in OH. Each row is the same as main text Fig. 2 but using a linear Gaussian inversion with varying uncertainty in the OH anomalies. Top row uses an uncertainty of 20%, middle row uses 10%, and bottom row uses 5%.

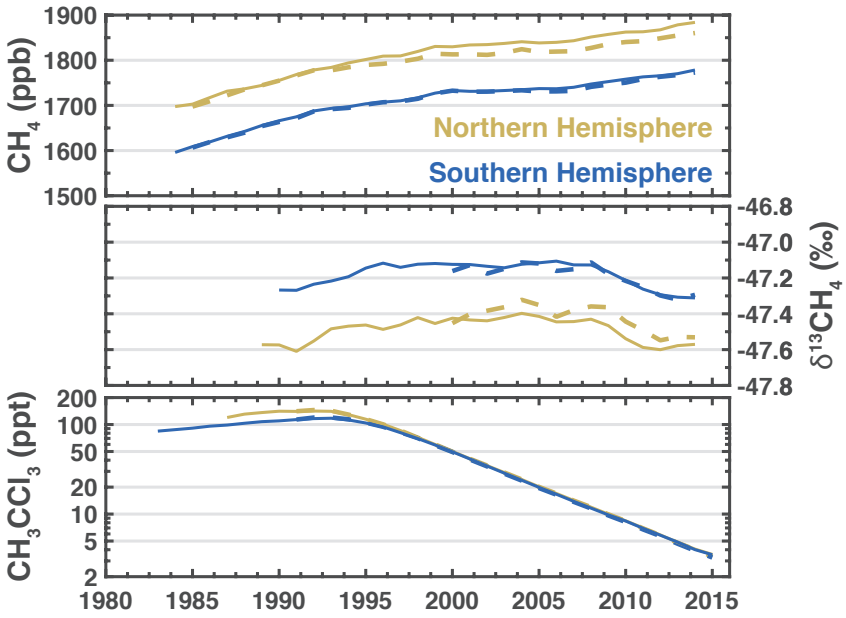

Figure 10: Comparison of the two hemispheric averaging schemes. Solid line is the bootstrapping scheme presented in Section 2 and dashed line is the alternate hemispheric average (E. Dlugokencky, NOAA/ESRL, personal communication; data included in tarball with code).

4.5 Varying the methyl chloroform reaction rate

We only consider the OH loss pathway for methyl chloroform (and methane). As such, the OH is representative of the entire loss term and induces an uncertainty in the appropriate reaction rate. The initial reaction rate was chosen to have a methyl chloroform lifetime of approximately 5.5 years[15], we use this as "Case A". We also test a case where we increased the methyl chloroform/OH reaction rate constant by 5%, resulting in a methyl chloroform lifetime of ∼5.3 years. The resulting methyl chloroform concentrations can be seen in the top row of Fig. S15 (simulated with the prior emissions).

Case A overestimates the methyl chloroform concentrations in the latter part of the record while Case B does a better job of simulating the methyl chloroform concentrations. However, there are also uncertainties in the methyl chloroform emissions in the latter part of the record. The prior emissions (dashed lines in the middle row of Fig. S15) shows that the prior assumes a simple exponential decay of the methyl chloroform emissions. A slightly faster rate of decay would also satisfy the methyl chloroform observations. This is exactly what happens in Case A. In Case A, the posterior emissions are reduced at a slightly faster rate than the prior emissions. The posterior simulations from both of these cases are able to reproduce the observations but they result in different emissions and OH anomalies (see Fig.16). We find that the change in the methane emissions and OH amonalies are about a factor of two less in Case B (reduced methyl chloroform lifetime).

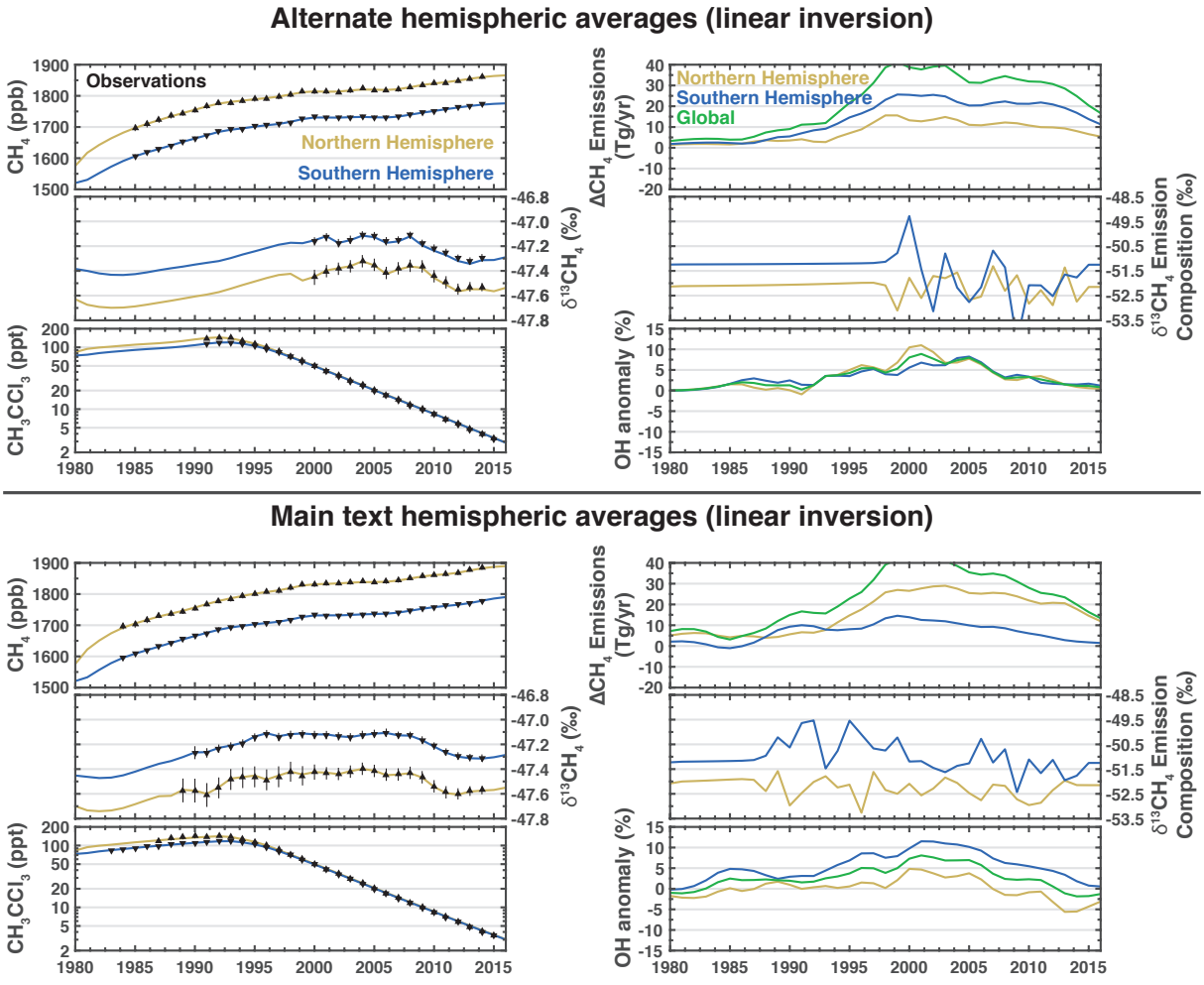

Figure 11: Linear Gaussian inversions with two different hemispheric averaging schemes. Top row uses the bootstrapping scheme presented in Section 2. Bottom row uses an alternate hemispheric averaging scheme (E. Dlugokencky, NOAA/ESRL, personal communication; data included in tarball with code).

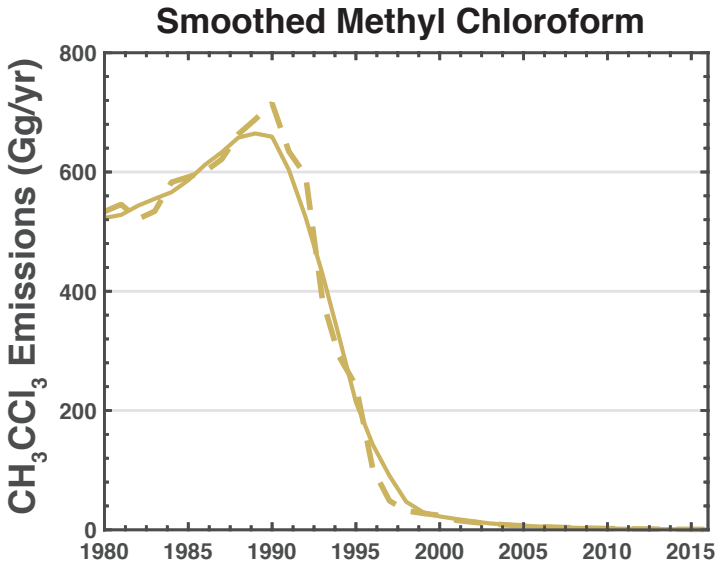

Figure 12: Smoothed methyl chloroform emissions. Dashed line is the emissions from Prinn *et al.*[14] and dashed line is smoothed using a 5-year filter.

5 Mechanistic explanation for the changes in OH

Changes in stratospheric ozone are a *potential* explanation for the decadal trends in OH. This is because changes in stratospheric ozone will affect $J\left(O^1D\right)$ and, in turn, tropospheric OH. Murray *et al.*[16] find that a 1% increase in stratospheric ozone leads to a 4.2% decrease in tropospheric OH (see Table 2 in Murray *et al.*[16]). Using this relationship and observations of stratospheric ozone from Mauna Loa (MLO), we can estimate the OH anomalies due to changes in stratospheric ozone.

Fig. 17 shows the OH anomalies inferred from stratospheric ozone at MLO, the OH anomalies from our "most likely solution", and the OH anomalies from McNorton *et al.*[17], Montzka *et al.*[18], and Rigby *et al.*[19]. While the magnitude of the OH anomalies inferred from stratospheric ozone at MLO is of the correct order the correlation is quite weak.

References

[1] Schaefer, H. *et al.* A 21st-century shift from fossil-fuel to biogenic methane emissions indicated by $^{13}CH_4$. *Science* **352**, 80–4 (2016).

[2] Rice, D. D. & Claypool, G. E. Generation, accumulation, and resource potential of biogenic gas. *Aapg Bulletin-American Association of Petroleum Geologists* **65**, 5–25 (1981).

[3] Martini, A. M., Budai, J. M., Walter, L. M. & Schoell, M. Microbial generation of economic accumulations of methane within a shallow organic-rich shale. *Nature* **383**, 155–158 (1996).

[4] Curtis, J. B. Fractured shale-gas systems. *Aapg Bulletin* **86**, 1921–1938 (2002).

[5] Stolper, D. A. *et al.* Gas formation. formation temperatures of thermogenic and biogenic methane. *Science* **344**, 1500–3 (2014).

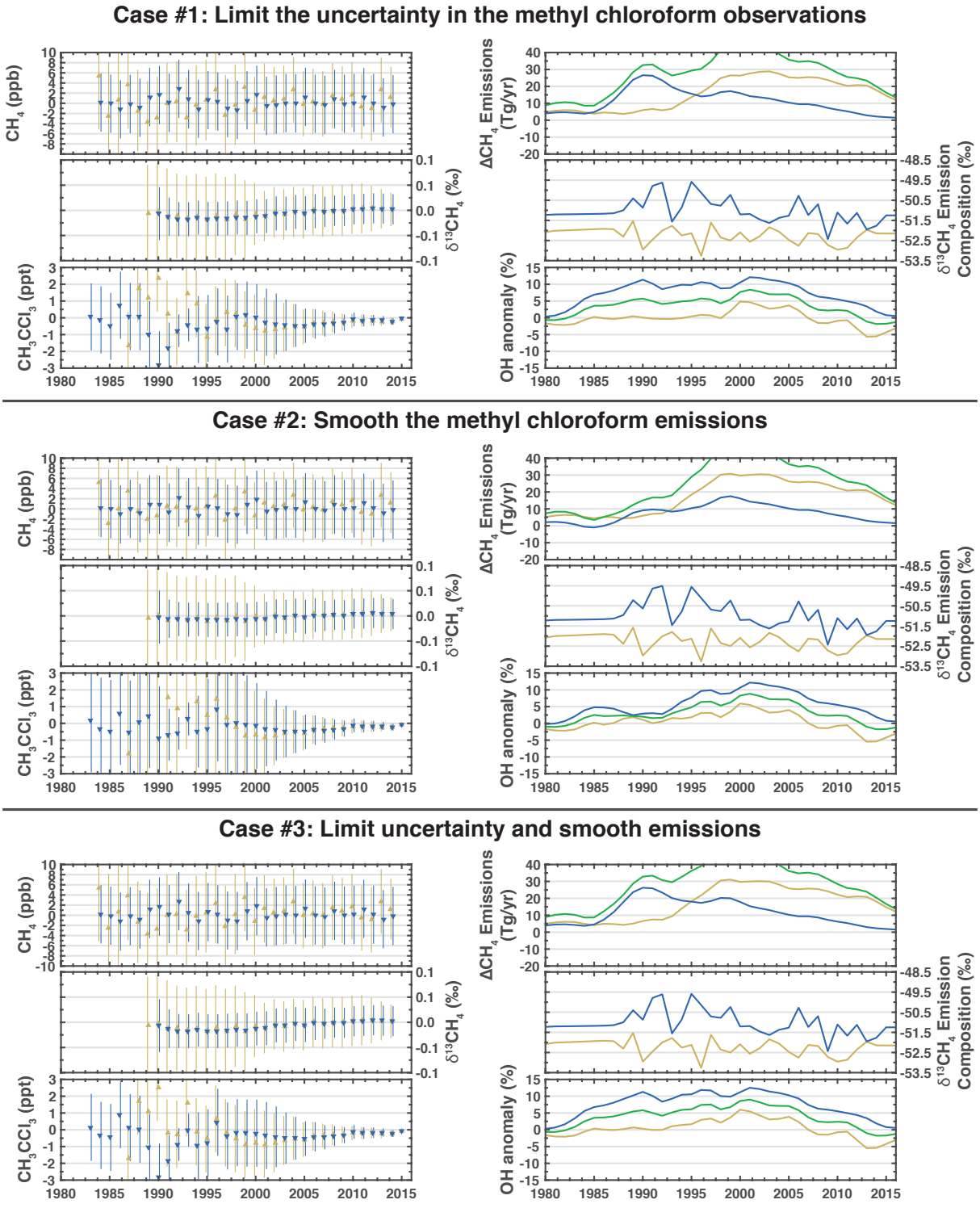

Figure 13: Results from the methyl chloroform sensitivity tests. Left column is the residuals and right column are the main drivers for the box model. Top panel is case 1. Middle panel is case 2. Bottom panel is case 3.

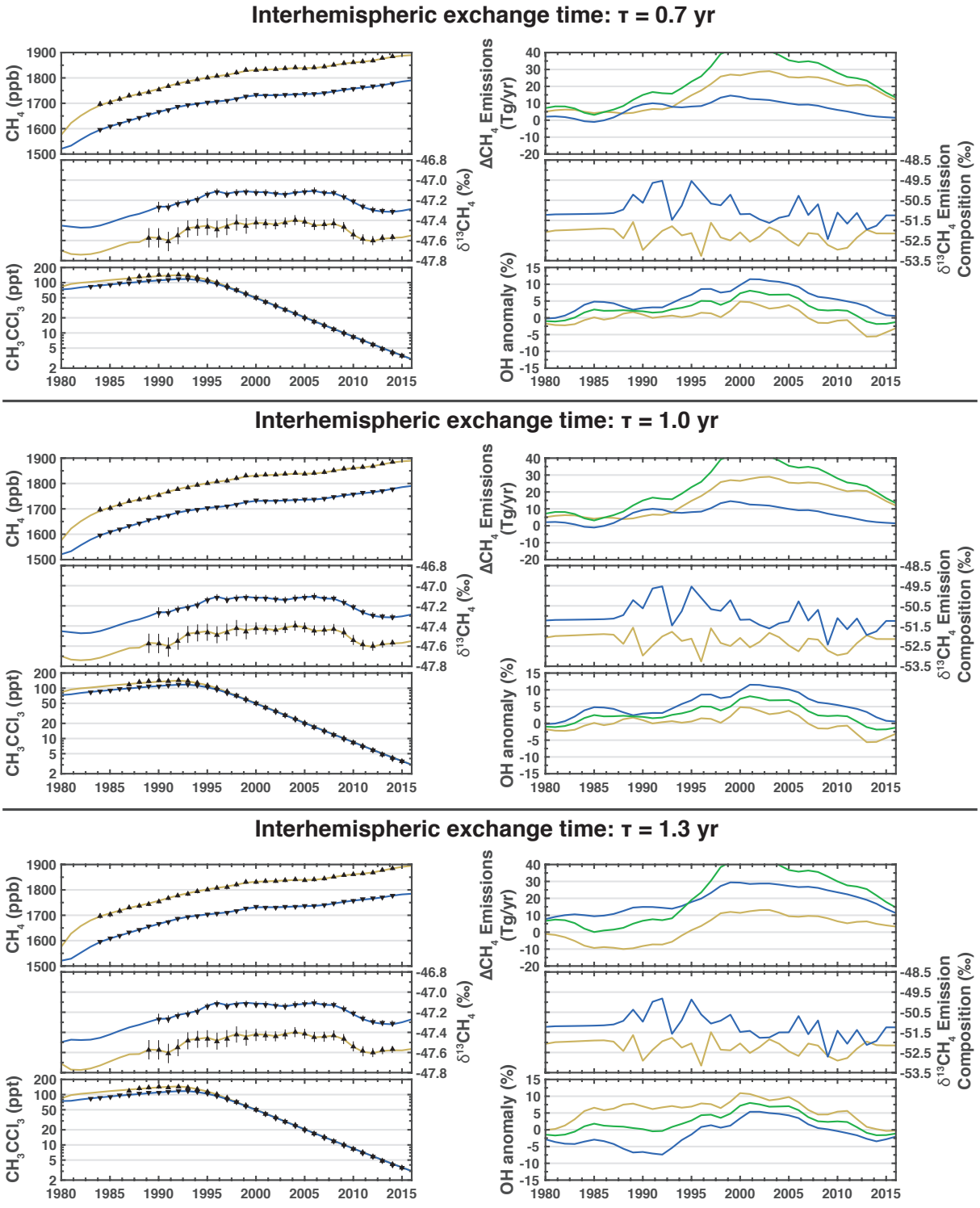

Figure 14: Varying the interhemispheric exchange time. Each row is the same as main text Fig. 2 but using a linear Gaussian inversion with varying interhemispheric exchange times (τ). Top row uses $\tau = 0.7$ yr, middle row uses $\tau = 1.0$ yr, and bottom row uses $\tau = 1.3$ yr.

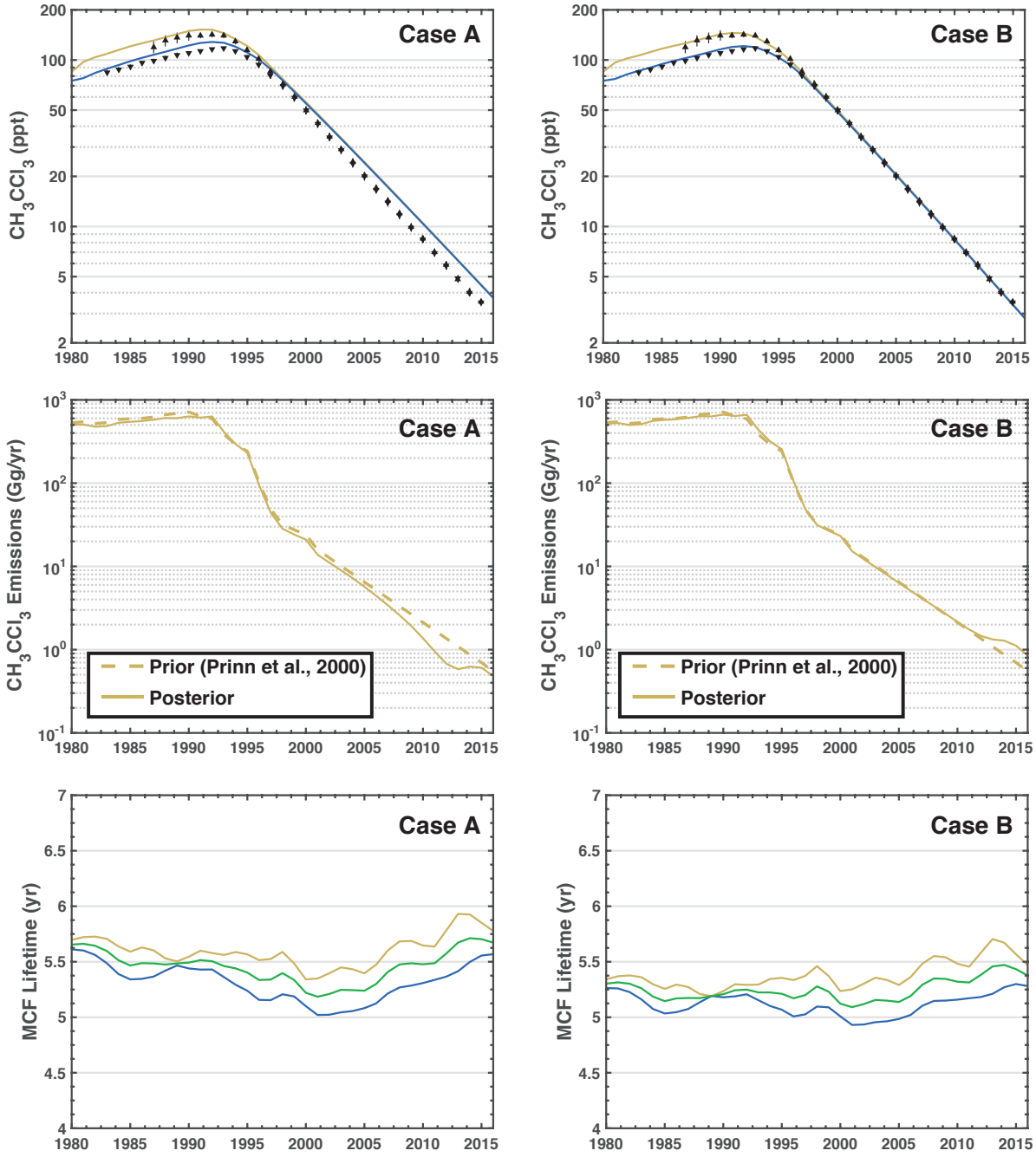

Figure 15: Varying the methyl chloroform reaction rate. Left column is with the Taldukar *et al.*[15] lifetime of 5.5 years and the right column is with a lifetime of ∼5.3 years. Top row shows the observed and simulated methyl chloroform observations. Middle row is the prior methyl chloroform emissions (dashed line) and posterior methyl chloroform emissions (solid line). Bottom panel is the methyl chloroform lifetimes in the posterior simulation.

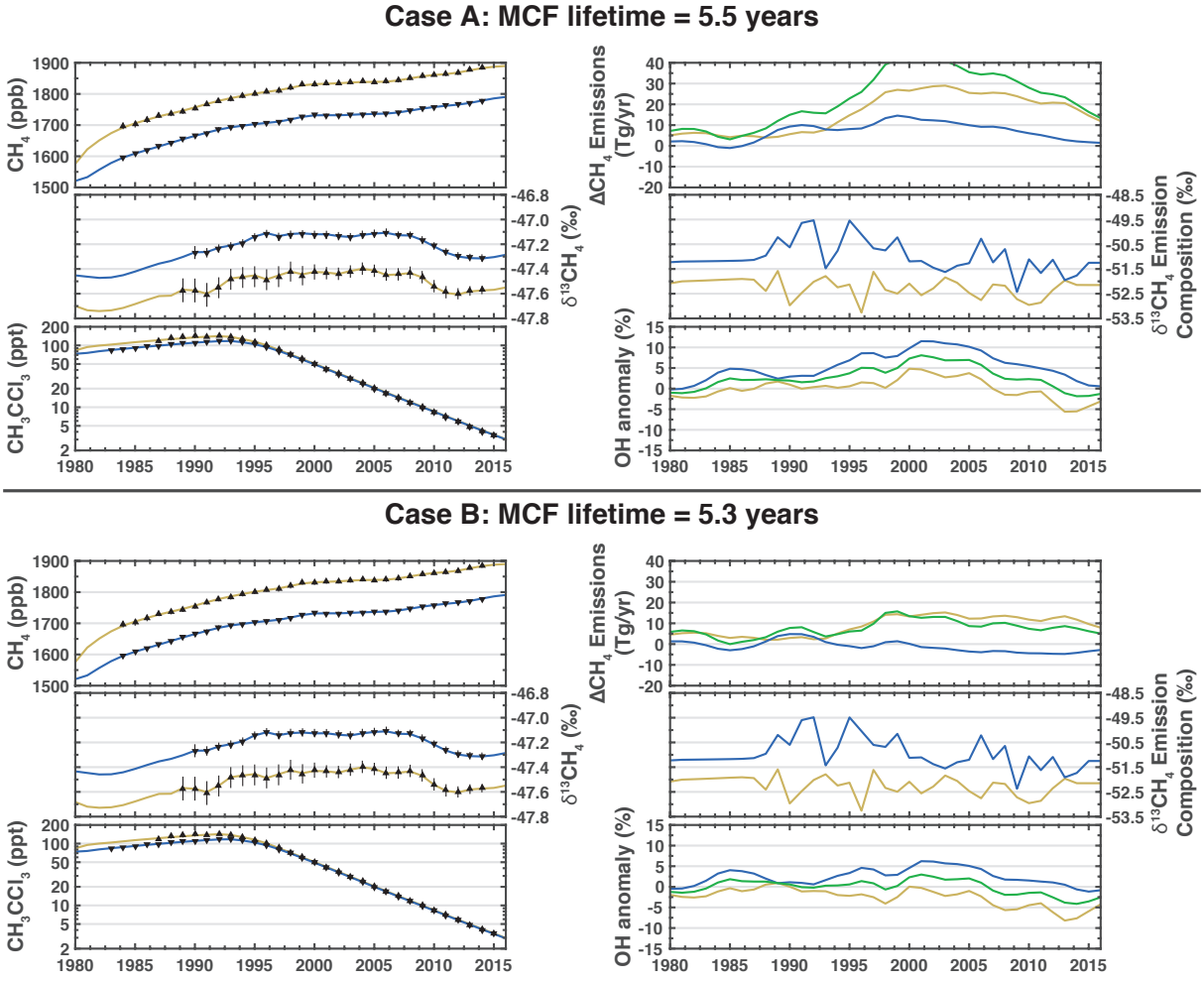

Figure 16: Varying the methyl chloroform reaction rate. Each row is the same as main text Fig. 2 but using a linear Gaussian inversion with varying methyl chloroform reaction rates. Top row results in a lifetime of 5.5 years[15] and the bottom row results in a lifetime of 5.3 years.

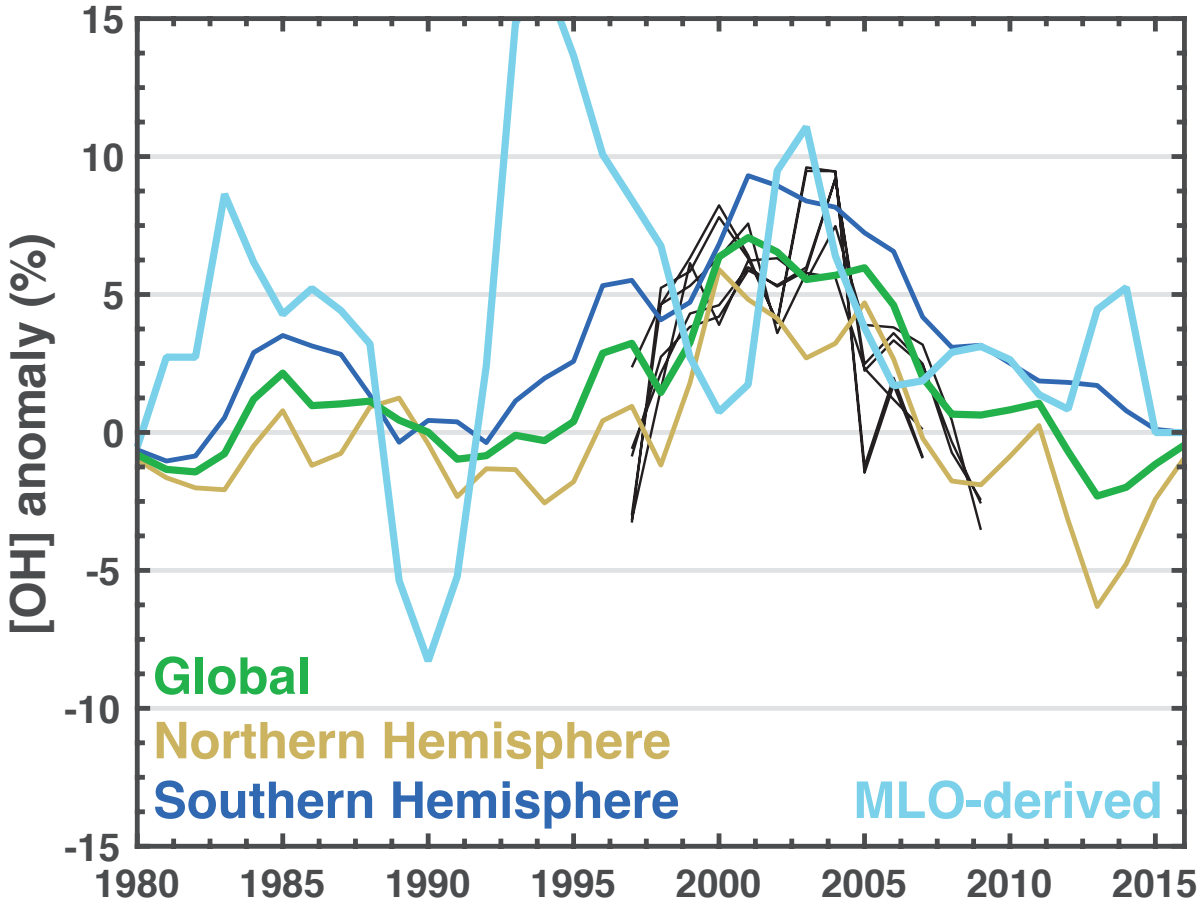

Figure 17: OH anomalies. Same as main text Fig. 3 but with the OH anomalies derived from stratospheric ozone observations at Mauna Loa (MLO-derived; cyan line).

[6] Wang, D. T. *et al.* Methane cycling. nonequilibrium clumped isotope signals in microbial methane. *Science* **348**, 428–31 (2015).

[7] Breas, O., Guillou, C., Reniero, F. & Wada, E. The global methane cycle: isotopes and mixing ratios, sources and sinks. *Isotopes Environ Health Stud* **37**, 257–379 (2001).

[8] Dlugokencky, E. J., Nisbet, E. G., Fisher, R. & Lowry, D. Global atmospheric methane: budget, changes and dangers. *Philos Trans A Math Phys Eng Sci* **369**, 2058–72 (2011).

[9] Schaefer, H. & Whiticar, M. J. Potential glacial-interglacial changes in stable carbon isotope ratios of methane sources and sink fractionation. *Global Biogeochemical Cycles* **22**, n/a–n/a (2008).

[10] Stolper, D. A. *et al.* Distinguishing and understanding thermogenic and biogenic sources of methane using multiply substituted isotopologues. *Geochimica et Cosmochimica Acta* **161**, 219–247 (2015).

[11] Schwietzke, S. *et al.* Upward revision of global fossil fuel methane emissions based on isotope database. *Nature* **538**, 88–91 (2016).

[12] Burkholder, J. B. *et al.* Chemical kinetics and photochemical data for use in atmospheric studies, evaluation no. 18. Tech. Rep., Jet Propulsion Laboratory (2015).

[13] Cantrell, C. A. *et al.* Carbon kinetic isotope effect in the oxidation of methane by the hydroxyl radical. *Journal of Geophysical Research-Atmospheres* **95**, 22455–22462 (1990).

[14] Prinn, R. G. *et al.* A history of chemically and radiatively important gases in air deduced from ALE/GAGE/AGAGE. *Journal of Geophysical Research: Atmospheres* **105**, 17751–17792 (2000).

[15] Talukdar, R. K. *et al.* Kinetics of the oh reaction with methyl chloroform and its atmospheric implications. *Science* **257**, 227–30 (1992).

[16] Murray, L. T., Logan, J. A. & Jacob, D. J. Interannual variability in tropical tropospheric ozone and OH: The role of lightning. *Journal of Geophysical Research: Atmospheres* **118**, 11,468–11,480 (2013).

[17] McNorton, J. *et al.* Role of OH variability in the stalling of the global atmospheric CH_4 growth rate from 1999 to 2006. *Atmospheric Chemistry and Physics* **16**, 7943–7956 (2016).

[18] Montzka, S. A. *et al.* Small interannual variability of global atmospheric hydroxyl. *Science* **331**, 67–9 (2011).

[19] Rigby, M. *et al.* Re-evaluation of the lifetimes of the major CFCs and CH_3CCl_3 using atmospheric trends. *Atmospheric Chemistry and Physics* **13**, 2691–2702 (2013).